Mechanical Engineering Advances 2023; 1(1): 94.
Original Research Article

Multigrid method for the solution of thermal elastohydrodynamic lubrication point contact problem with surface asperities

Vishwanath B. Awati[*], Parashuram M. Obannavar, Mahesh Kumar Nanjaiah

Department of Mathematics, Rani Channamma University, Belagavi 591156, India

*** Corresponding author:** Vishwanath B. Awati, awati.vb@rcub.ac.in

ARTICLE INFO

Received: 2 September 2023
Accepted: 6 October 2023
Available online: 15 October 2023

doi: 10.59400/mea.v1i1.94

ABSTRACT: The paper presents the numerical investigation of point contact thermal elasto-hydrodynamic lubrication (EHL) with surface asperities analyzed. The effect of temperature and surface roughness on fluid film thickness is studied in detail. The governing equations comprise Reynolds, film thickness, load balance, and energy equations with appropriate boundary conditions. The second-order finite difference approximation is used to discretize the governing equations, and the resultant nonlinear system of algebraic equations is solved using the Multigrid V-cycle with full approximation scheme (FAS) technique. The multi-level multi-integration (MLMI) technique is employed to solve the film thickness equation. The obtained results are illustrated in the form of graphs and tables that are comparable with earlier findings. The film thickness profiles show dimples near the outlet region due to the temperature-viscosity wedge mechanism. Isothermal minimum film thickness is higher than the thermal minimum film thickness. Minimum film thickness is much smaller due to the slide-to-roll ratio being positive as compared to negative, whereas the behavior of central film thickness is in contrast to that of minimum film thickness.

KEYWORDS: thermal; EHL; multigrid method; FAS; slide to roll ratio; MLMI

1. Introduction

The thermal effect plays a vital role in tribo components such as gears, cams, tappets, rolling bearings, etc. For these components, the load is applied over a small contact region, which results in high pressure generated within the contact region, which leads to deforming the contacting surfaces. This phenomenon of lubrication is widely known as elasto-hydrodynamic lubrication (EHL). The simulation of EHL point contact is able to understand the failure of these components, and temperature is a key factor in galling or scuffing of these components. The effects of pressure, temperature, and film thickness are influenced by the surface roughness of the contacting surfaces that are viewed on a microscopic level.

In 1961, Crook[1] theoretically studied the hydrodynamic line contact problem by the mechanism of heat generation and removal in oil film. Sternlicht et al.[2] examined the fluid behavior in the contact area and understood the impact of lubricant on rolling contact fatigue life. The numerical solution of coupled Reynolds, elasticity, and energy equations was analyzed through mean viscosity across fluid film, as discussed by Cheng and Sternlicht[3]. Dowson and Whitker[4] used numerical methodology for the solution of the EHL problem due to the impact of sliding on the performance of EHL contact; further, the relation between temperature and pressure distribution was analyzed. Murch and Wilson[5] deliberated the viscous heat instead of the conventional Reynolds equation in the inlet region of the EHL problem and noticed that constriction in the film thickness is due to viscous heating. The thermal EHL of an elliptical contact problem was numerically elucidated using the finite difference method with viscosity and density depending on pressure, as analyzed by Bruggemann and Kollmann[6].

The detailed analysis of the thermal EHL point contact problem was discussed by Kim and Sadeghi[7,8] by considering pure rolling and low slip conditions in order to get the solution. Further work reveals the importance of shear heating under pure rolling/sliding conditions and predicts that shear heating is in the Hertzian zone. Salehizadeh and Saka[9], Wolff and Kubo[10] and Kazama et al.[11] scrutinized the thermal EHL line contact problem by adopting a parabolic cross-film temperature profile to reduce the three-dimensional problem into a two-dimensional problem as well as the discretization cost of the energy equation. The thermal EHL circular contact problem was analyzed using the Multigrid method to determine the solution of Reynolds and film thickness equations under pure rolling/sliding conditions, as discussed by Lee et al.[12]. Ehret et al.[13] debated the thermal EHL elliptical contact problem and adopted Lee et al.[12] numerical procedure to understand the effects of spin on elliptical contacts and also noticed that high temperature across the fluid film. Qu et al.[14] determined the occurrence of steady-state dimple phenomenon is due to temperature-viscosity wedge mechanism on thermal EHL circular contacts, and Yang et al.[15] confirm the occurrence of steady-state dimple. Guo et al.[16] numerically studied the thermal EHL circular contact problem by considering slide-to-roll ratio, which is more than 2 as calculated, and also predicted the formation of dimples, behavior of traction, and variations of dimples, which are compared with experimental findings. Kim et al.[17] debated the thermal EHL circular contact problem with a Newtonian fluid by using the moving heat source equation given by Carslaw and Jaeger numerically by the multigrid technique. The non-Newtonian thermal EHL circular contact problem was analyzed numerically by Kim et al.[18] and attained the results, which are compared with experimental findings of Cann and Spikes[19]. The Erying model was implemented for the thermal EHL point contact problem by Liu et al.[20] and they introduced a novel technique to calculate the effective viscosity of Erying fluid.

Generally, there are no completely smooth surfaces in machine components. Many researchers have investigated the impact of surface topography on EHL contacts, and this surface topography was laconically known as micro-EHL. The surface area includes longitudinal, transverse, and isotropic. The isotropic uncouth describes no apparent directions and is randomly distributed. The surface roughness influences hydrodynamic fluid flow entraining action, which in turn impacts lubricating performance. The surface roughness collision can be analyzed by using statistical models, viz., stochastic and deterministic models.

The stochastic model considers only a few numbers of statistical parameters to reveal the impact of surface roughness on contacts and fluids. Greenwood and Williamson[21] showed that the deformation mainly depends on the topography of the surface and introduced the criterion to differentiate the surfaces that touch elastically from those that touch plastically. Greenwood and Tripp[22] introduced the general theory of contact between two rough plane surfaces. Patir and Chang[23] used a stochastic model to explore the effect of surface roughness on hydrodynamic lubrication. And defined the average Reynolds equation for rough surfaces and defined it in terms of pressure and shear flow factors. The deterministic model was used to understand the surface roughness on the EHL line contact problem, which was discussed by Sadeghi and Sui[24]. Chang[25] numerically evaluated the thermal EHL problem with rolling/sliding contacts on rough surfaces by using the Newton-Raphson method, and the energy equation was solved using the control volume finite element method. Hu and Zhu[26] determined the numerical solution of the mixed EHL point contact problem and further computed 3-D surface roughness under different rolling/sliding conditions. Wang et al.[27] analyzed the mixed EHL problem by considering Patir and Chang[23] average flow, and the obtained results are compared with those of Hu and Zhu[26]. The improvements in EHL, together with surface roughness interaction, give rise to a new methodology for predicting the Stribeck curve. Lu et al.[28] reported the results of a series of experiments conducted on journal bearings together with a theoretical prediction of the stribeck-type behavior. And these were compared with the results of the mixed EHL model for line contact, which are in good agreement with experiment findings.

The deterministic model is used to solve thermal EHL circular and elliptical contact problems numerically to compute pressure and temperature of mixed lubrication discussed by Deolalikar et al.[29]. Yang et al.[30] studied the thermal EHL elliptical contact problem for rolling/sliding conditions with a non-Newtonian fluid model by considering both transverse and longitudinal surface roughness. And conclude that thermal and non-Newtonian effects can be enlarged significantly by the surface waviness. The impact of surface roughness on friction coefficients was discussed by Akbarzadeh and Khonsari[31]. Sojoudi and Khonsari[32] analyzed the EHL point contact problem by considering rough surfaces and estimated the friction coefficient behavior under different operating parameters. Zhu and Wang[33] studied the deterministic model for mixed lubrication of EHL lines and circular and elliptical contact problems to verify the performance of lubricating films. Masjedi and Khonsari[34] deliberated the inclusion of surface roughness in EHL point contact; a statistical-based elasto-plastic model was used to investigate the influence of surface roughness. The isothermal EHL point contact problem with bio-based oil as lubricant on smooth and rough surface asperity was numerically studied by Awati et al.[35] further concluding that the bio-based product brings out an alternative source of lubricant to reduce the energy crises. Zhang et al.[36] presented the point contact thermal EHL problem with zero entrainment velocity (ZEV) by considering both the Newtonian and Erying models. The impact of transversely oriented ridges was analyzed through thermal EHL, and the impact of ridges on pressure, film thickness, friction coefficients, and temperatures was studied by Cui et al.[37]. Awati et al.[38] studied the thermal EHL line contact problem numerically by using the multigrid method through the full approximation scheme (FAS) technique with bio-based oil as lubricant. And noticed that the reduction in the minimum film thickness for high speed and shown pressure spike as a function of relevant operating parameters. The size effect on EHL of roller pairs considering both Newtonian and Erying fluid thermal EHL problems under steady state was discussed by Liu et al.[39] further, concluded that the size effect is more pronounced in thermal elastohydrodynamic lubrication (TEHL) as compared to isothermal EHL. Hulqvist et al.[40] studied the effect of surface roughness on the EHL contact problem in order to improve the durability and friction performance of machine elements. The concept of how the slip effects temperature rise and its coupling effect with heat are still unknown. But researchers like Zhao et al.[41] discussed the effect of boundary slip on the thermal EHL point contact problem. And studied the coupled effects on boundary slip and heat on EHL contacts under large slide-to-roll ratios. The influence of the dimension change of the bushpin on the pressure, oil film thickness, temperature rise, and traction coefficient in the contact zone using the thermal EHL model of finite line contact was analyzed by Zhang et al.[42]. Zhang et al.[43] discussed the variations of oil film pressure, thickness, and temperature rise in the contact zone of plate pin pairs in silent chains numerically. In order to understand the interplay of boundary slip and heat, Zhao and Wong[44] used the complete thermal EHL of a non-wetting/wetting contact under high slide-to-roll ratios.

1.1. Multigrid method

Most of the computational modelling in engineering problems often involves the solution of systems of linear/nonlinear algebraic equations, which are represented in the form of matrix. The computation of the problem becomes difficult whenever there are a there are a large number of unknowns or an increase in the size of the coefficient matrix. The solution of these equations by direct method via. The Gaussian elimination method is computationally intensive and involves round-off errors. Iterative methods offer alternative tools because they provide the solution with minimum roundoff errors and are more amenable to parallel processing. Iterative methods such as Gauss-Seidel have a few drawbacks, viz., slow convergence due to the accumulation of round-off errors or low-frequency error components that are not removed efficiently after certain iterations. These methods also require starting with good or near-initial approximations so that the convergence becomes faster or is achieved with a smaller number of iterations, which is not possible in the case of nonlinear problems.

The multigrid method is a powerful iterative method that circumvents the convergence of the problems of other iterative methods. This method uses iteration on a variety of grid sizes or matrix sizes to speed up the convergence of the solution. Further, the method has many applications in a wide range of problems, including the solution of differential and integral equations. The Gauss-Seidel iteration method slows down the convergence as the grid size increases. The multigrid method prevents slow convergence on grids of different sizes; thus, it substantially reduces all frequency error components.

Brandt[45] introduced the multigrid method to solve large systems of linear as well as non-linear algebraic equations. Lubrecht et al.[46] adopted the multigrid method for the solution of the EHL point contact problem. Later, Venner[47] introduced the dipole Jacobi relaxation technique to enhance the performance of the multigrid method. The relaxation scheme is the main feature of this method that determines the efficiency of the method and decreases the error components. The main advantages of this method are that the convergence speed is independent of discretization points. Two types of relaxation schemes are employed in this technique; one of the schemes is Jacobi distributive line relaxation, which is applied to domains where pressure is more pronounced in the contact region. Another one is Gauss-Seidel relaxation, which is applied where the pressure is less severe, i.e., to inlet and outlet regions.

Full Approximation Scheme (FAS) algorithm

Multigrid is a powerful iterative method that converges much faster as compared to other iterative methods. This method eliminates high-frequency error components on the finer grid with only a few number of relaxation sweeps, whereas low-frequency error components are unaltered with further or more number of relaxation sweeps. By restriction operator is used to determine the solution to coarser grid, the low frequency error components act as high frequency error components and are easily eliminated with a few number of relaxation sweeps. Thus, the solution is obtained at a finer grid by using prolongation added to the solution to get a more approximate solution. The procedure is repeated until the convergence is achieved. The algorithm of the multigrid method comprising two grids is as follows.

- The system of non-linear algebraic equations are represented as

$$L^{\hat{\hbar}}(\breve{u})^{\hat{\hbar}} = f^{\hat{\hbar}},$$

where, L denotes the nonlinear operator, $\breve{u}$is the exact solution and $f$is the right hand side function, $\hat{\hbar}$ represents the fine grid mesh.

- Residual at the fine grid can be computed as

$$\nabla^{\hat{\hbar}} = f^{\hat{\hbar}} - L^{\hat{\hbar}}\left(\breve{v}^{\hat{\hbar}}\right), e^{\hat{\hbar}} = \breve{u}^{\hat{\hbar}} - \breve{v}^{\hat{\hbar}},$$

where, $\breve{v}$ is the approximate solution to the exact solution$\breve{u}$.

- Thus, residual and current approximate solution can be restricted to coarse grid as

$$\nabla^{2\hat{\hbar}} = I_{\hat{\hbar}}^{2\hat{\hbar}}\nabla^{\hat{\hbar}} = I_{\hat{\hbar}}^{2\hat{\hbar}}\left(f^{\hat{\hbar}} - L^{\hat{\hbar}}\left(\breve{v}^{\hat{\hbar}}\right)\right) \text{ and } \breve{v}^{2\hat{\hbar}} = I_{\hat{\hbar}}^{2\hat{\hbar}}\breve{v}^{\hat{\hbar}},$$

where $I_{\hat{\hbar}}^{2\hat{\hbar}}$ is restrict operator.

- Then compute the coarse grid as

$$L^{2\hat{\hbar}}\left(\breve{u}^{2\hat{\hbar}}\right) = L^{2\hat{\hbar}}\left(\breve{v}^{2\hat{\hbar}}\right) + \nabla^{2\hat{\hbar}}$$

- Now, solve the coarser grid approximation to error as $e^{2\hat{\hbar}} = \breve{u}^{2\hat{\hbar}} - \breve{v}^{2\hat{\hbar}}$. In the next step interpolate the error approximation to fine grid and correct the current fine grid approximation as

$$\breve{v}^{\hat{\hbar}} \leftarrow \breve{v}^{\hat{\hbar}} + I_{2\hat{\hbar}}^{\hat{\hbar}}e^{2\hat{\hbar}}$$

where, $I_{2\hat{\hbar}}^{\hat{\hbar}}$ is prolongation operator.

- Apply two to three Gauss-Seidel relaxation sweeps in order to get more approximate solution.

The present work mainly focuses on the thermal behavior of the EHL point contact problem and also analyzes the surface roughness effect under thermal conditions. The study encompassed Reynolds, film thickness, and energy equations; these equations were solved simultaneously by using the multigrid technique with a Gauss-Seidel relaxation process with a low relaxation factor employed, and film thickness equations were solved by using the multi-level multi-integration (MLMI) method, and the Gauss-Seidel iteration process was used to solve the energy equation.

2. Governing equations

The physical configuration of governing equations characterizes lubrication conditions materialize between a ball and plane. The circumferential velocity $u_2$of the ball and plane is moving with velocity u_1 is parallel tou_2 and the axes of the system are placed at centre of the contact. The x-axis is the same orientation as the entering velocity, although the z-axis is aimed perpendicular from surface 1 to surface 2.

2.1. Reynolds equation

The Reynolds equation for the EHL point contact regime is the same as Lee et al.[12] and across fluid film thickness, the lubricant properties are assumed to be constant; also, the lubricant acts as a Newtonian fluid. The viscosity and density are dependent on both pressure and mean temperature of the film. As a consequence, the thermal Reynolds equation reads as,

$$\frac{\partial}{\partial x}\left(\frac{\rho\hbar^3}{\eta}\frac{\partial p}{\partial x}\right) + \frac{\partial}{\partial y}\left(\frac{\rho\hbar^3}{\eta}\frac{\partial p}{\partial y}\right) - 12\bar{u}\frac{\partial(\rho\hbar)}{\partial x} = 0, \text{ where } \bar{u} = \frac{u_1+u_2}{2} \tag{1}$$

The dimensionless parameters used in this study are

$$X = \frac{x}{a};\ Y = \frac{y}{a};\ P = \frac{p}{p_{\hbar}};\ H = \frac{\hbar R}{a^2};\ \rho^* = \frac{\rho}{\rho_0};\ \eta^* = \frac{\eta}{\eta_0};\ U = \frac{\eta_0\bar{u}}{ER};\ W = \frac{w}{E'R^2};\ \widehat{W} = \frac{\widehat{w}}{a};\ T^* = \frac{T}{T_0};\ M = W(2U)^{-3/4};\ L = G(2U)^{1/4};\ G = \alpha E;\ SR = \frac{2(u_1 - u_2)}{u_1 + u_2} \tag{2}$$

By using Equation (2) in Equation (1), the dimensionless Reynolds equation becomes

$$\frac{\partial}{\partial X}\left(\varepsilon\frac{\partial P}{\partial X}\right) + \frac{\partial}{\partial X}\left(\varepsilon\frac{\partial P}{\partial Y}\right) - \lambda\frac{\partial(\bar{\rho}H)}{\partial X} = 0 \tag{3}$$

where $\lambda = \frac{12\eta_0 \bar{u} R^2}{a^3 p_\hbar}$, $\varepsilon = \frac{\bar{\rho} H^3}{\eta^*}$, and boundary conditions for Equation (3) is given as;

At the inlet region $P(X_{in}, Y) = 0$; At the outlet region $P(X_{out}, Y) = 0$, $\frac{\partial P(X_{out}, Y)}{\partial X} = 0$; and at the two sides $P|_{Y=\pm 2} = 0$.

The viscosity-pressure-temperature relation proposed by Roelands et al.[48] used to incorporate the change in viscosity along with pressure and temperature expressed as

$$\eta = \eta_0\, exp\{[ln(\eta_0 - 9.67)][-1 + (1 + 5.1 \times 10^{-9} p)^z] - \gamma(T - T_0)\} \tag{4}$$

where, γ denotesthe temperature-viscosity coefficient, η_0 is the inlet viscosity of lubricant, T is the temperature and T_0 denotes the initial temperature. The dimensionless form of Equation (4) becomes

$$\eta^* = exp\{[ln(\eta_0 - 9.67)][-1 + (1 + 5.1 \times 10^{-9} p_\hbar P)^z] - \gamma(T^* - 1)\} \tag{5}$$

Dowson and Higginson[49] proposed density-pressure relation is adopted with modifications to the effect of temperature is given as,

$$\rho = \rho_0 \left(1 + \frac{0.6 \times 10^{-9} p}{1 + 1.7 \times 10^{-9} p}\right)[1 - \beta(T - T_0)] \tag{6}$$

where, β is the thermal expansivity. The dimensionless form of Equation (6) can be expressed as

$$\bar{\rho} = \left(1 + \frac{0.6 \times 10^{-9} p_\hbar P}{1 + 1.7 \times 10^{-9} p_\hbar P}\right)[1 - \beta(T^* - 1)] \tag{7}$$

2.2. Film thickness equation

Consider two bodies that are elastic and semi-infinite; also, the deformation of the bounding surface is taken into consideration. The radii of curvature of the ball are greater than the contact length; for an undeformed surface, the parabolic approximation is adopted. The point contact EHL film thickness equation is given by

$$\hbar(x,y) = \hbar_{00} + \frac{x^2}{2R} + \frac{y^2}{2R} + \frac{2}{\pi E'} \int_{-\infty}^{\infty} \int_{-\infty}^{\infty} \frac{p(x', y')dx'\, dy'}{\sqrt{(x - x')^2 + (y - y')^2}} + \mathfrak{R}(x,y) \tag{8}$$

The dimensionless form of Equation (8) can be written as

$$H(X,Y) = H_{00} + \frac{X^2 + Y^2}{2} + \frac{2}{\pi^2} \int_{-\infty}^{\infty} \int_{-\infty}^{\infty} \frac{P(X', Y')dX'\, dY'}{\sqrt{(X - X')^2 + (Y - Y')^2}} + \mathfrak{R}(X,Y) \tag{9}$$

where $\mathfrak{R}(X,Y) = \bar{A}\, cos\left(\frac{2\pi \hat{X}}{\hat{W}}\right)$, $\hat{X} = X\, cos(\varphi) - Y\, sin(\varphi)$, $\hat{W} = \bar{w}/b$ denotes the dimensionless wavelength, $\bar{A} = amp/\hbar_\hbar$ denotes the non-dimensional amplitude, $\hbar_\hbar = b^2/R$ denotes maximum Hertzian deformation, φ denotes the orientation angle.

2.3. Force balance equation

The force balance equation with respect to point contact problem becomes

$$\int_{-\infty}^{\infty} \int_{-\infty}^{\infty} p(x,y)dxdy - w = 0 \tag{10}$$

The dimensionless form of Equation (10) becomes

$$\int_{-\infty}^{\infty} \int_{-\infty}^{\infty} P(X,Y)dXdY = \frac{2\pi}{3} \tag{11}$$

2.4. Energy equation

The detailed study of energy equation for a Newtonian fluid is given by Pai[50] and Liu[51]. The temperature distribution within the fluid film shall be computed from the solution of energy equation by considering convective term in the present study.

$$c_p\rho\left(u\frac{\partial T}{\partial x}+v\frac{\partial T}{\partial y}-w\frac{\partial T}{\partial z}\right)=ku\frac{\partial^2 T}{\partial z^2}-\frac{T}{\rho}\frac{\partial\rho}{\partial T}\left(u\frac{\partial p}{\partial x}+vu\frac{\partial p}{\partial y}\right)+\eta\left[\left(\frac{\partial u}{\partial z}\right)^2+\left(\frac{\partial v}{\partial z}\right)^2\right] \tag{12}$$

The dimensionless form of Equation (12) can be expressed as

$$\begin{gathered}\frac{c_p\rho_0 E^{\prime}\ a^3}{\eta_0 kR}\left(\bar{\rho}U^*\frac{\partial T^*}{\partial X}+\bar{\rho}V^*\frac{\partial T^*}{\partial Y}\right)-\frac{c_p\rho_0 E^{\prime}\ a^2}{\eta_0 k}\bar{\rho}W^*\frac{\partial T^*}{\partial Z}=\frac{\partial^2 T^*}{\partial Z^2}-\frac{E^{\prime}\ p_{\hbar}a^3}{\eta_0 kT_0R}\frac{\partial\bar{\rho}}{\partial T^*}\frac{1}{\bar{\rho}}\\ \left(U^*\frac{\partial P}{\partial X}+V^*\frac{\partial P}{\partial Y}\right)T^*+\frac{E^{\prime\,2}R^2}{k\eta_0T_0}\left[\left(\frac{\partial U^*}{\partial Z}\right)^2+\left(\frac{\partial V^*}{\partial Z}\right)^2\right]\eta^*\end{gathered} \tag{13}$$

where

$$U^*=U_1^*+\frac{p_{\hbar}a^3}{R^3E'}\frac{\partial P}{\partial X}\left(\int_0^Z\frac{Z}{\eta^*}dZ-\frac{\int_0^H(Z/\eta^*)dZ^2}{\int_0^H(1/\eta^*)dZ}\int_0^Z\frac{1}{\eta^*}dZ\right)+\frac{U_2^*-U_1^*}{\int_0^H(1/\eta^*)dZ}\int_0^Z\frac{1}{\eta^*}dZ \tag{13a}$$

$$V^*=\frac{p_{\hbar}a^3}{R^3E'}\frac{\partial P}{\partial Y}\left(\int_0^Z\frac{Z}{\eta^*}dZ-\frac{\int_0^H(Z/\eta^*)dZ}{\int_0^H(1/\eta^*)dZ}\int_0^Z\frac{1}{\eta^*}dZ\right) \tag{13b}$$

The dimensionless temperature boundary condition for upper surface may be expressed as

$$T_{up}^*=\frac{k\sqrt{\eta_0R}}{\sqrt{\pi\rho_1c_1k_1u_1E'a^3}}\int_{-\infty}^X\left(\frac{\partial T^*}{\partial Z}\right)_{Z=0}\frac{dS}{\sqrt{X-S}}+1 \tag{14}$$

The temperature boundary condition for the lower surface may be expressed in dimensionless form as

$$T_{dw}^*=\frac{k\sqrt{\eta_0R}}{\sqrt{\pi\rho_2c_2k_2u_2E'a^3}}\int_{-\infty}^X\left(\frac{\partial T^*}{\partial Z}\right)_{Z=H}\frac{dS}{\sqrt{X-S}}+1 \tag{15}$$

3. Method of solution

3.1. Discretization of governing equations

The governing mathematical modelling of physical equations, viz. Reynolds, film thickness, load balance, and energy equations, is discretized by using second-order finite difference approximations. The domain of computation is $[X_{in}, X_{out}]=[-4, 1.5]$, $[Y_{in}, Y_{out}]=[-2, 2]$ and Equation (3) can be discretized as

$$\begin{gathered}\left(\frac{\xi_{i-1/2,j}P_{i-1,j}-\left(\xi_{i-1/2,j}+\xi_{i+1/2,j}\right)P_{i,j}+\xi_{i+1/2,j}P_{i+1,j}}{\Delta X^2}\right)\\ +\left(\frac{\xi_{i,j-1/2}P_{i,j-1}-\left(\xi_{i,j-1/2}+\xi_{i,j+1/2}\right)P_{i,j}+\xi_{i,j+1/2}P_{i,j+1}}{\Delta Y^2}\right)\\ -\left(\frac{\bar{\rho}_iH_i-\bar{\rho}_{i-1}H_{i-1}}{\Delta X}\right)=0,\end{gathered} \tag{16}$$

where $\xi=\frac{\varepsilon}{\lambda}$. The film thickness Equation (9) can be discretized as

$$H_{i,j} = H_{00} + \frac{X_i^2}{2} + \frac{Y_j^2}{2} + \frac{2}{\pi^2}\sum_{k=1}^{N}\sum_{l=1}^{N} K_{i,j,k,l}P_{k,l} - \bar{A}\,cos\left(\frac{2\pi X'_{j}}{\hat{W}}\right) \tag{17}$$

where $K_{i,j,k,l}$ denotes the kernel and is given by Venner and Lubrecht[52].

$$\begin{aligned} K_{i,j,k,l} = {} & -|X_p|\,arcsin\,\hbar\left(\frac{Y_p}{X_p}\right) + |Y_p|\,arcsin\,\hbar\left(\frac{X_p}{Y_p}\right) - |X_m|\,arcsin\,\hbar\left(\frac{Y_p}{X_m}\right) - |Y_p|\,arcsin\,\hbar\left(\frac{X_m}{Y_p}\right) \\ & - |X_p|\,arcsin\,\hbar\left(\frac{Y_m}{X_p}\right) - |Y_m|\,arcsin\,\hbar\left(\frac{X_p}{Y_m}\right) + |X_m|\,arcsin\,\hbar\left(\frac{Y_m}{X_m}\right) \\ & + |Y_m|\,arcsin\,\hbar\left(\frac{X_m}{Y_m}\right) \end{aligned} \tag{18}$$

and $X_p = X_k - X_i + \frac{\Delta X}{2}$; $X_m = X_k - X_i - \frac{\Delta X}{2}$; $Y_p = Y_l - Y_j + \frac{\Delta Y}{2}$; $Y_m = Y_l - Y_j - \frac{Y}{2}$.

The energy equation represented in Equation (13) can be written as

$$\begin{aligned} & \frac{\partial^2 T^*}{\partial Z^2} + A_2\left(\bar{\rho}U^*\frac{\partial T^*}{\partial X} + \bar{\rho}V^*\frac{\partial T^*}{\partial Y}\right) - 2A_5\bar{\rho}W^*\frac{\partial T^*}{\partial Z} + A_3\frac{1}{\bar{\rho}}\left(U^*\frac{\partial P}{\partial X} + V^*\frac{\partial P}{\partial Y}\right)T^* \\ & = A_4\left[\left(\frac{\partial U^*}{\partial Z}\right)^2 + \left(\frac{\partial V^*}{\partial Z}\right)^2\right]\eta^* \end{aligned} \tag{19}$$

The discretized form of Equation (19) as

$$\begin{aligned} & \frac{1}{\Delta Z^2}(T_{k-1}^* - 2T_k^* + T_{k+1}^*) - A_5\bar{\rho}W_k^*\frac{1}{\Delta Z}(T_{k+1}^* - T_{k-1}^*) + A_3\left(U_k^*\frac{\partial P}{\partial X} + V_k^*\frac{\partial P}{\partial Y}\right)\frac{T_k^*}{\bar{\rho}_k} \\ & + A_2\left(\bar{\rho}_k U_k^*\frac{T_{i,j,k}^* - T_{i-1,j,k}^*}{\Delta X} + \bar{\rho}_k V_k^*\frac{T_{i,j,k}^* - T_{i,j-1,k}^*}{\Delta Y}\right) = A_4\left[\left(\frac{\partial U^*}{\partial Z}\right)^2 + \left(\frac{\partial V^*}{\partial Z}\right)^2\right]\eta_k^* \end{aligned} \tag{20}$$

where $A_2 = \left(\frac{-c\rho E'a^3}{\eta_0 kR}\right)$, $A_3 = \left(\frac{-E'p_{\hbar}a^3 D}{\eta_0 kR}\right)$, $A_4 = \left(\frac{E'^2 R^2}{\eta_0 kT_0}\right)$, $A_5 = \left(\frac{-c\rho_0 E'a^2}{2\eta_0 k}\right)$.

By omitting the subscripts *i, j.* in Equation (20) and it can be written as

$$A_{1,k}T_{k-1}^* + A_{2,k}T_k^* + A_{3,k}T_{k+1}^* = A_{4,k} \tag{21}$$

where $= 2, 3, 4, \ldots N_Z - 1$. $A_{1,k} = \frac{1}{\Delta Z^2} + A_5\bar{\rho}_k W_k^*\frac{1}{\Delta Z}$,

$$A_{2,k} = -2\frac{1}{\Delta Z^2} + A_2\bar{\rho}_k\frac{1}{\Delta X}(U_k^* + V_k^*) + A_3\frac{1}{\bar{\rho}_k}\left(U_k^*\frac{\partial P}{\partial X} + V_k^*\frac{\partial P}{\partial Y}\right),\ A_{3,k} = \frac{1}{\Delta Z^2} - A_5\bar{\rho}_k W_k^*\frac{1}{\Delta Z},$$

$$A_{4,k} = A_4\left[\left(\frac{\partial U^*}{\partial Z}\right)^2 + \left(\frac{\partial V^*}{\partial Z}\right)^2\right]\eta_k^* + A_2\bar{\rho}_k\frac{1}{\Delta X}\left(U_k^* T_{i-1,j,k}^* + V_k^* T_{i,j-1,k}^*\right).$$

The temperature boundary conditions are discretized as

$$A_{1,N_Z}T_{N_Z-1}^* + A_{2,N_Z}T_{N_Z}^* = A_{4,N_Z} \tag{22}$$

where $A_{1,N_Z} = 1 + \frac{4}{3}A_6\sqrt{\Delta X}\frac{N_Z - 1}{H}$, $A_{2,N_Z} = -\frac{4}{3}A_6\sqrt{\Delta X}\frac{N_Z - 1}{H}$, $A_{4,N_Z} = 1 - A_6\sqrt{\Delta X}\frac{N_Z - 1}{H}C_{C1}$.

The discretized form of Equation (11) becomes

$$\Delta X \Delta Y \sum_{i=1}^{N}\sum_{j=1}^{N} P_{i,j} = \frac{2\pi}{3} \tag{23}$$

The inlet boundary condition is $P(X_{in}, Y) = 0$ and the outlet negative pressure is set to zero. The discretized boundary conditions are

$$P(X_{in}, Y) = 0 \text{ and } \frac{P(X_{out}, Y) - P(X_{out-1}, Y)}{\Delta X} = 0 \tag{24}$$

and the side boundary conditions becomes $P(X, Y = \pm 2) = 0$.

3.2. Solution procedure

For this problem, at each grid level pressure is relaxed by applying Gauss-Seidel relaxation scheme. Let us denote $(LP)_{i,j}$by $L_{i,j}\ P$ represents algebraic equation for pressure on each grid level and it can be written as

$$L_{i,j}(P) = F_{i,j}\left(i = 1, 2, 3,\ \ldots n_x, j = 1,2,3,\ \ldots n_{y-1}\right).$$

Let $c_1$be an under relaxation factor, the process for pressure iteration can be expressed as

$$\hat{P}_{i,j} = \bar{P}_{i,j} + c_1\delta_{i,j},$$

where $\delta_{i,j} = \left(\frac{\partial L_{i,j}}{\partial P_{i,j}}\right)^{-1} r_{i,j}$,

$$\begin{aligned} r_{i,j} = F_{i,j} - \left[\xi_{i-1/2,j}\hat{P}_{i,j} - \left(\xi_{i-1/2,j} + \xi_{i+1/2,j}\right)\bar{P}_{i,j} + \xi_{i+1/2,j}P_{i,j}\right]\frac{1}{\Delta X^2} \\ - \begin{bmatrix} \xi_{i,j-1/2}\hat{P}_{i,j-1} - \left(\xi_{i,j-1/2} + \xi_{i,j+1/2}\right)\hat{P}_{i,j} \\ +\xi_{i,j+1/2}\hat{P}_{i,j+1} \end{bmatrix}\frac{1}{\Delta Y^2} + \left(\bar{\rho}_{i,j}\bar{H}_{i,j} - \bar{\rho}_{i-1}\hat{H}_{i-1,j}\right)\frac{1}{\Delta X}, \end{aligned}$$

$$\left(\frac{\partial L_{i,j}}{\partial P_{i,j}}\right) = -\left(\xi_{i-1/2,j} + \xi_{i+1/2,j}\right)\frac{1}{\Delta X^2} - \left(\xi_{i,j-1/2} + \xi_{i,j+1/2}\right)\frac{1}{\Delta Y^2} - \frac{2}{\pi^2}\left(\bar{\rho}_{i,j}K_{ij,ij}^{\Delta\Delta\Delta} - \bar{\rho}_{i-1,j}K_{i-1j,ij}^{\Delta\Delta\Delta}\right),$$

where $\hat{P}_{i,j}, \hat{P}_{i-1,j}$ and $\hat{H}_{i,j}, \hat{H}_{i-1,j}$ are the previous iteration values and are replaced by $\bar{P}_{i,j}$ and $\bar{H}_{i,j}$ are the new values of pressure and film thickness respectively. After computing pressure from the FAS scheme, the MLMI method is employed to obtain deformation with initial pressure and temperature. The obtained pressure is used to solve the energy equation by using finite difference with the Gauss-Seidel iteration method. The obtained temperature from the energy equation is used to solve the Reynolds equation for pressure and compute temperature using the updated pressure. The procedure is continued until the convergence criteria is satisfied, i.e.,

$$\frac{\sum\left|\bar{P}_{i,j} - \hat{P}_{i,j}\right|}{\sum\bar{P}_{i,j}} \leq 1 \times 10^{-04}, \frac{\sum\left|\bar{T}_{i,j}^{*} - \hat{T}_{i,j}^{*}\right|}{\sum\bar{T}_{i.j}^{*}} \leq 1 \times 10^{-05}.$$

where $\bar{T}^*$ is the updated temperature value and $\hat{T}^*$ is previous temperature value.

4. Results and discussion

The EHL point contact problem lubricated with Newtonian fluid and surface roughness is examined numerically by using the multigrid method with the FAS technique. The governing Reynolds and load balance equations are solved using the FAS scheme, and the film thickness equation is solved by using the MLMI technique, and energy equation is solved by using the Gauss-Seidel iteration scheme. These equations are simultaneously solved to get pressure, film thickness, and temperature profiles. For the present numerical computation, 5-V cycles are used in order to get the solution with 64 × 64 grid points.

Table 1 shows the physical parameters used in the present study which include both solid and lubricant properties. The comparison of isothermal results of central and minimum film thickness with thermal film thickness are illustrated in **Table 2**, and obtained results are compared with Hamrock and Dowson[53] empirical formula, and the results agree very well.

Table 1. Solid and lubricants properties.

Parameters	**Values**
Ambient viscosity	0.04
Equivalent radius	0.16
Elastic modulus(GPa)	206
Inlet temperature of the lubricant (K)	303

Table 1. (*Continued*).

Parameters	**Values**
Thermal conductivity of surfaces(W/mK)	46
Thermal conductivity of lubricant (W/mK)	0.14
Density (Kg/m^3)	7850
Specific heat of contact solids	470
Specific heat of lubricant (J/KgK)	2000
Ambient density (Kg/m^3)	890
Density of surfaces (Kg/m^3)	2000
Temperature-viscosity coefficient	−1.1
Temperature-density coefficient of lubricant (K^{-1})	−0.00065

Table 2. Minimum and central film thickness values are compared with Hamrock and Dowson empirical values for different loads.

Load M	**Isothermal film thickness**		**Thermal film thickness**		**Hamrock and Dowson**[53]	
	H_{min}	H_{cen}	H_{min}	H_{cen}	H_{min}	H_{cen}
40	0.6199	0.2450	0.1688	0.2585	0.0989	0.1634
60	0.1190	0.1807	0.1178	0.1944	0.0733	0.1213
100	0.0730	0.1258	0.0729	0.1335	0.0502	0.0834

Figures 1 and **2** illustrate the isothermal and thermal film thickness distributions for loads varying from $M = 20$ to 100 with constant speed $L = 12.04$, it is observed that the occurrence of dimples in the thermal film thickness is due to the temperature-viscosity wedge mechanism. The contour plots of isothermal and thermal film thickness distributions show a horse shoe constriction; the minimum film thickness present in the side lobes is noticed, and it is shown in **Figures 3** and **4**, respectively, for varying loads $M = 20$ to 100 with constant speed $L = 12.04$. The comparison between isothermal and thermal film thickness contours is also depicted, with a slide-to-roll ratio of 0.25. **Figures 5** and **6** predict the isothermal and thermal pressure distribution profiles for different loads ranging from $M = 20$ to 100 for constant speed $L = 12.04$ with SR = 0.25. It is perceived that pressure spike decreases with an increase in load parameter. Also, both isothermal and thermal pressure and film thickness profiles are demonstrated in **Figure 7** for various loads $M = 20, 40, 80, 100$ at a constant speed $L = 12.04$.

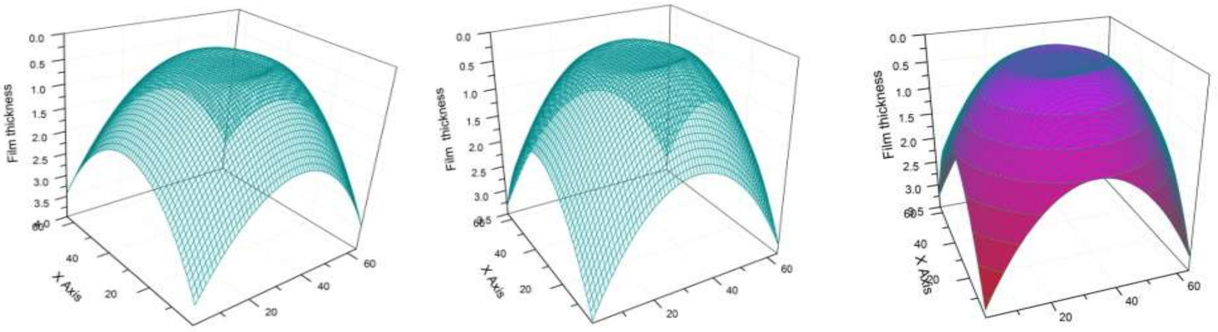

M = 20 *M* = 40 *M* = 60

Figure 1. (*Continued*).

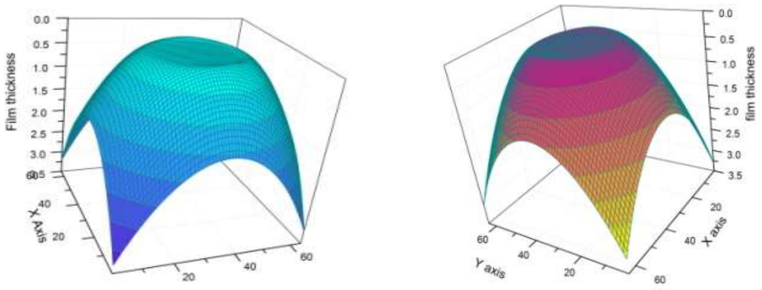

M = 80 *M* = 100

Figure 1. Isothermal film thickness profiles for varying load from M = 20 to 100 with constant speed *L* = 12.04.

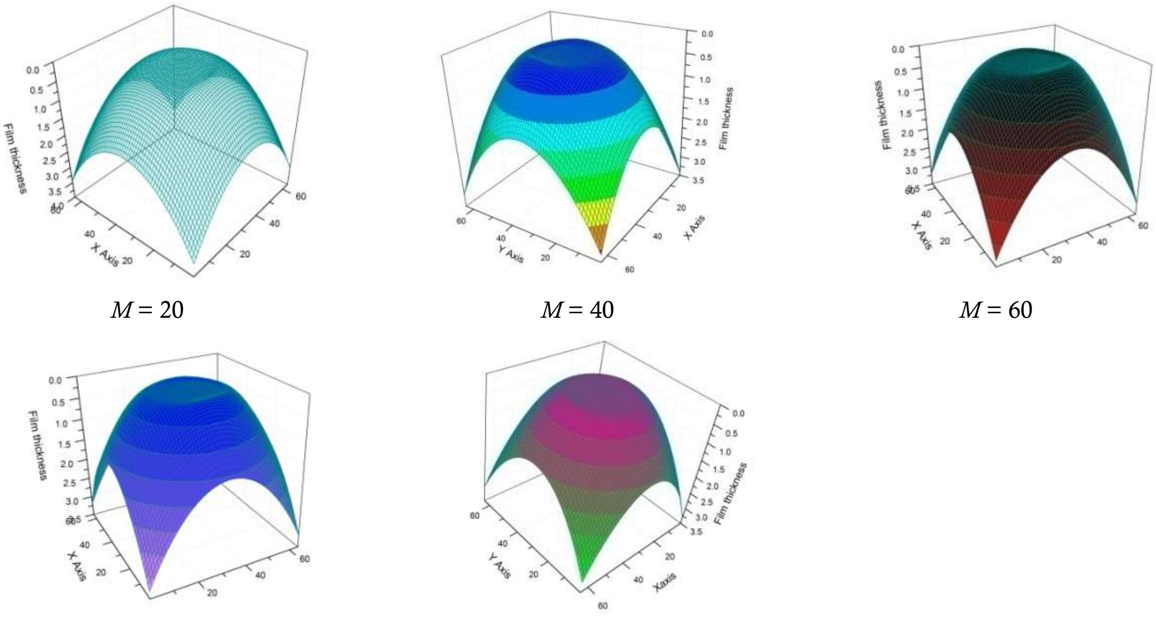

M = 20 *M* = 40 *M* = 60

M = 80 *M* = 100

Figure 2. Thermal film thickness profiles for varying load from *M* = 20 to 100 with the constant speed *L* = 12.04.

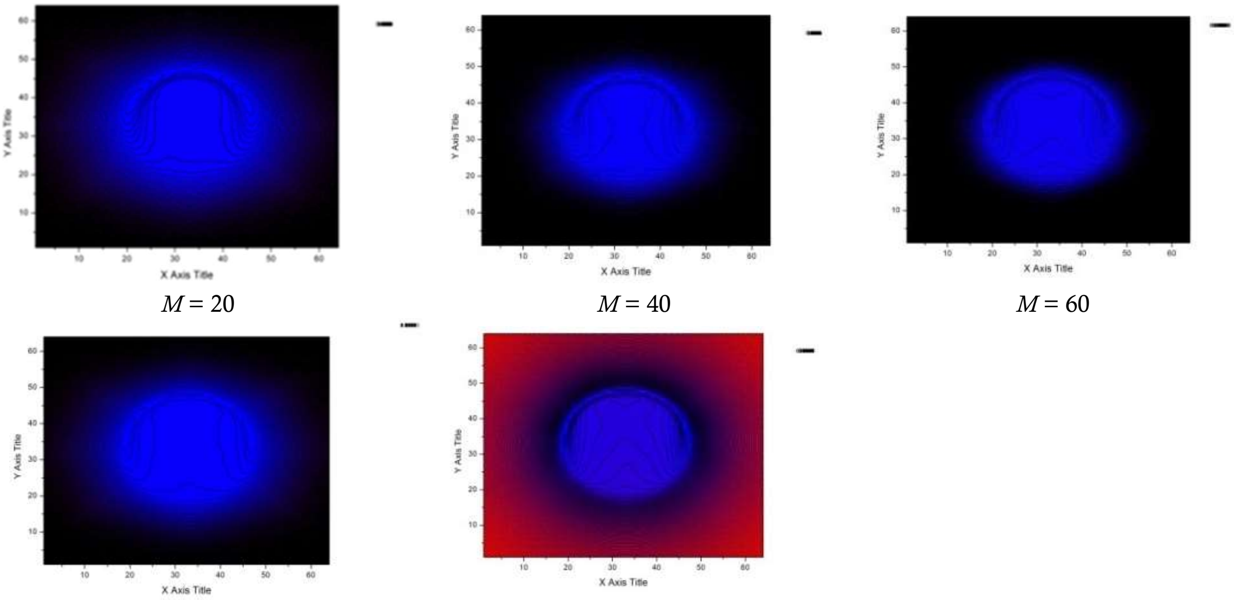

M = 20 *M* = 40 *M* = 60

M = 80 *M* = 100

Figure 3. Contour plot of isothermal film thickness profiles for varying load from *M* = 20 to 100 with the constant speed *L* = 12.04.

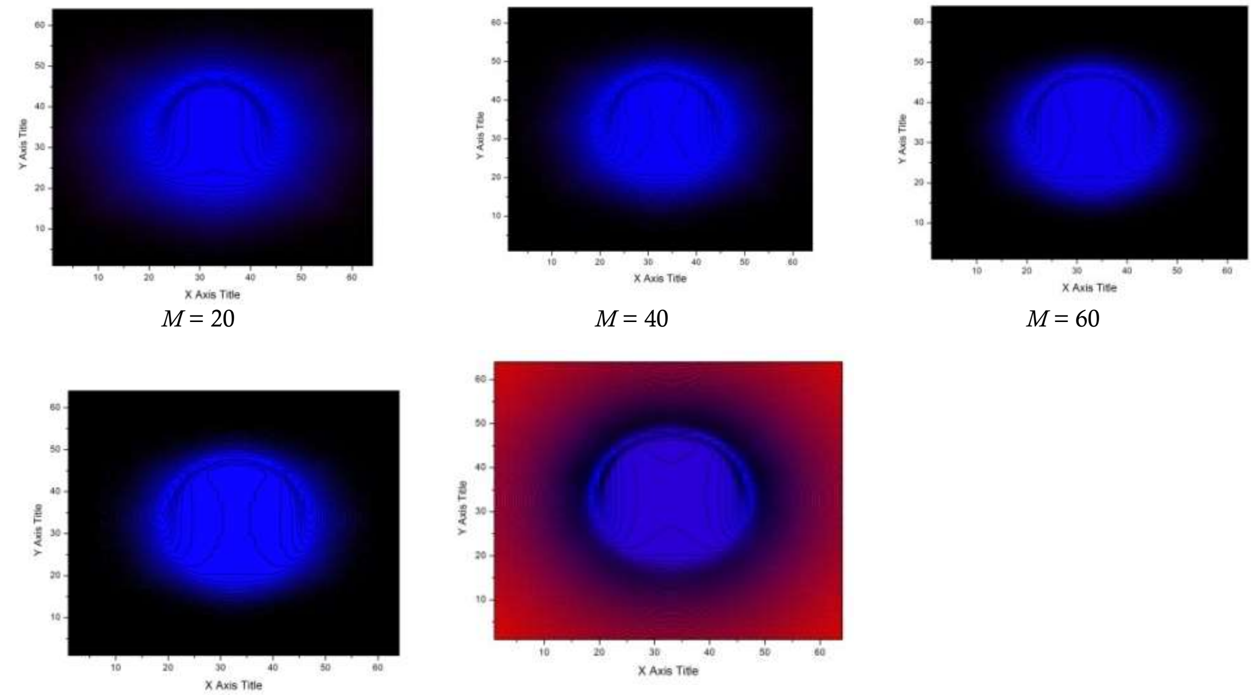

$M = 20$ $M = 40$ $M = 60$

$M = 80$ $M = 100$

Figure 4. Contour plot of thermal film thickness profiles for varying load from $M = 20$ to 100 with the constant speed $L = 12.04$.

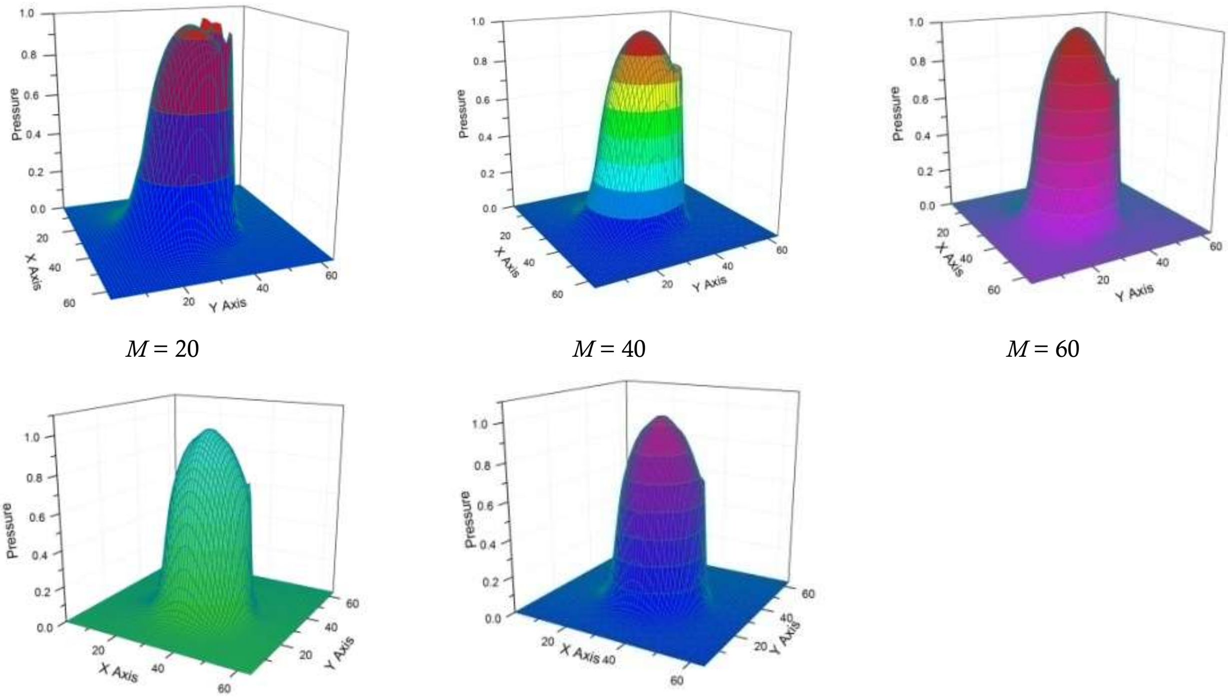

$M = 20$ $M = 40$ $M = 60$

$M = 80$ $M = 100$

Figure 5. Isothermal pressure distributions for varying load from $M = 20$ to 100 with the constant speed $L = 12.04$.

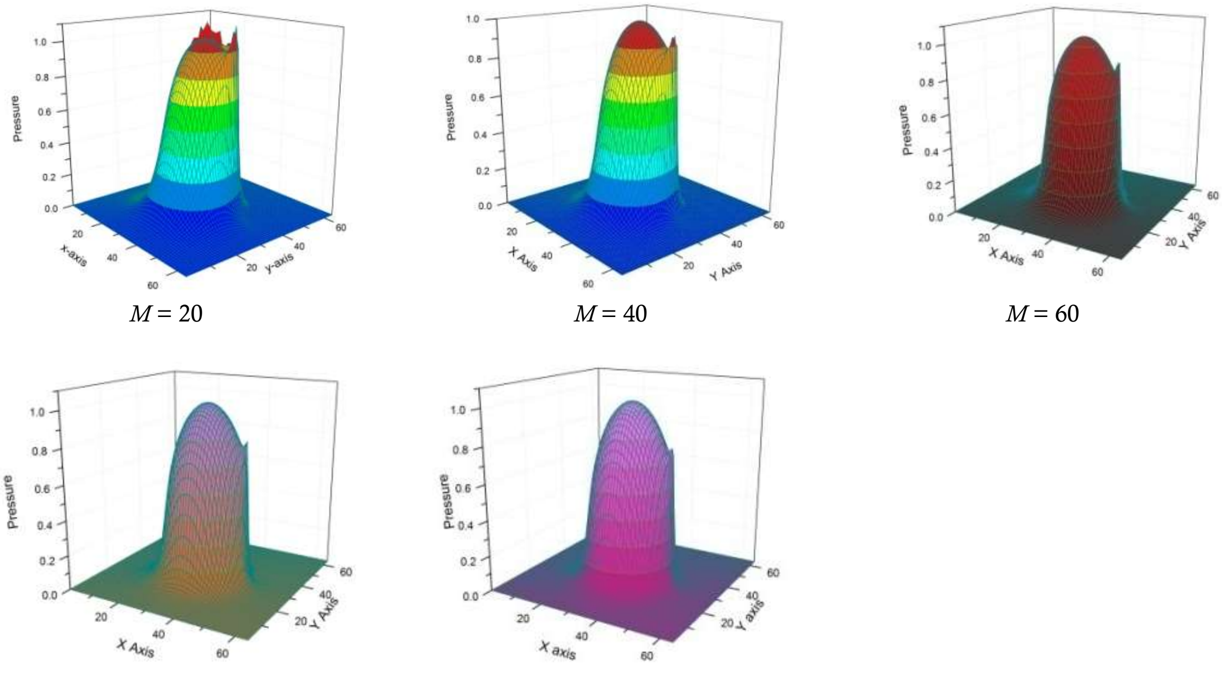

M = 20 *M* = 40 *M* = 60

M = 80 *M* = 100

Figure 6. Thermal pressure distributions for varying load from *M* = 20 to 100 with the constant speed *L* = 12.04.

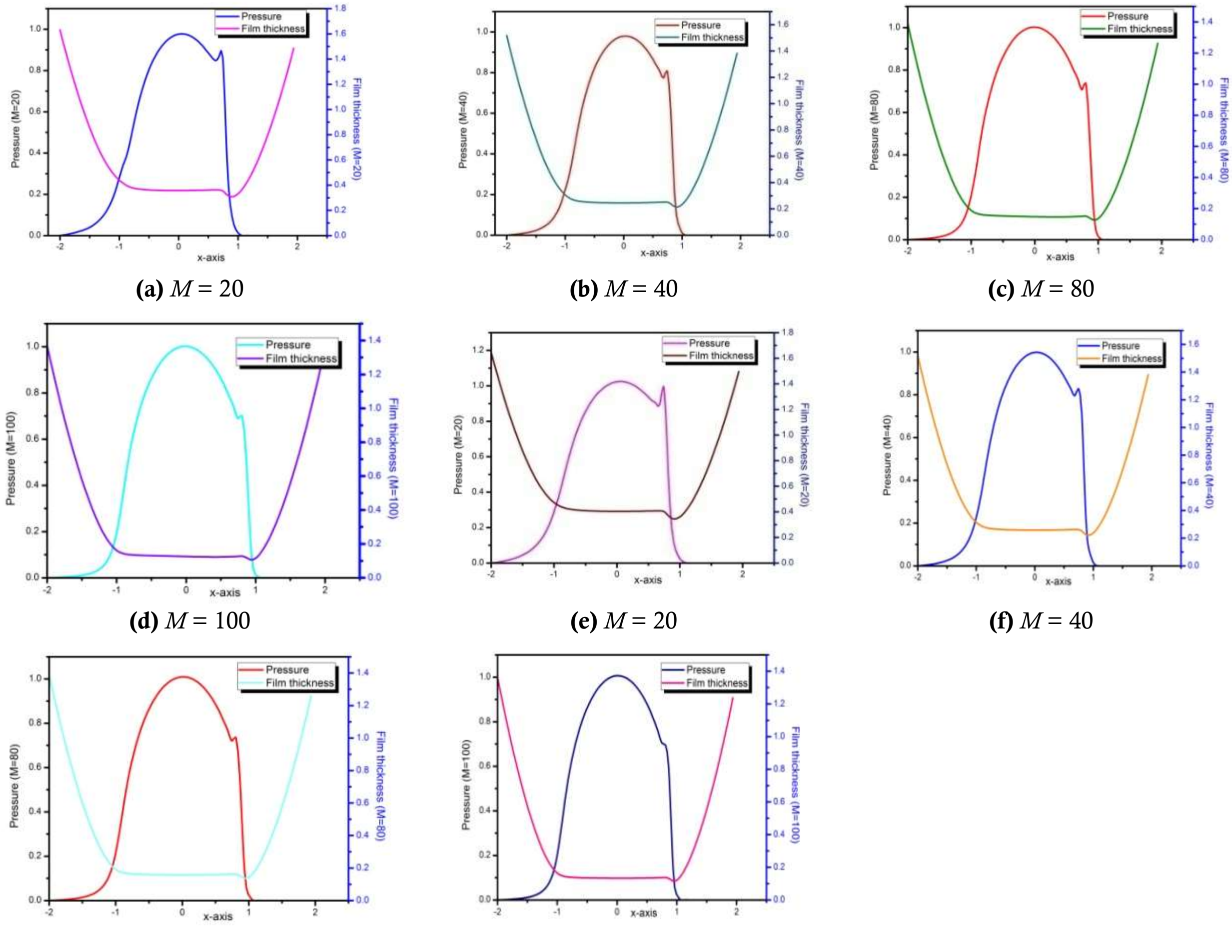

(a) *M* = 20 **(b)** *M* = 40 **(c)** *M* = 80

(d) *M* = 100 **(e)** *M* = 20 **(f)** *M* = 40

(g) *M* = 80 **(h)** *M* = 100

Figure 7. (a)–(d) represent the isothermal pressure and film thickness profiles; and **(e)–(h)** represent thermal pressure and film thickness profiles for varying load from *M* = 20 to 100 with the constant speed *L* = 12.04.

Figures 8 and **9** show the mid-film temperature distributions and are exemplified in layer-wise temperature profiles. It envisages that mid-film temperature is much higher than that of surface temperatures; also, the mid-film temperature is portrayed in layer 3, and surface temperatures are shown in layers 1 and 2, as described in **Figure 9**, with varying loads $M = 20 - 100$ with $L = 12.04$ and a slide-to-roll ratio of 0.25. For varying speed from $L = 13.05, 13.63, 14.27, 14.83$ with constant load $M = 20$ and a slide-to-roll ratio of 0.25, **Figures 10a–h** demonstrate the pressure distributions with constant load $M = 20$. The pressure spike increases with an increase in speed, and comparisons between isothermal and thermal pressure distributions are presented in **Figures 10a–d** and **Figures 10e–h**.

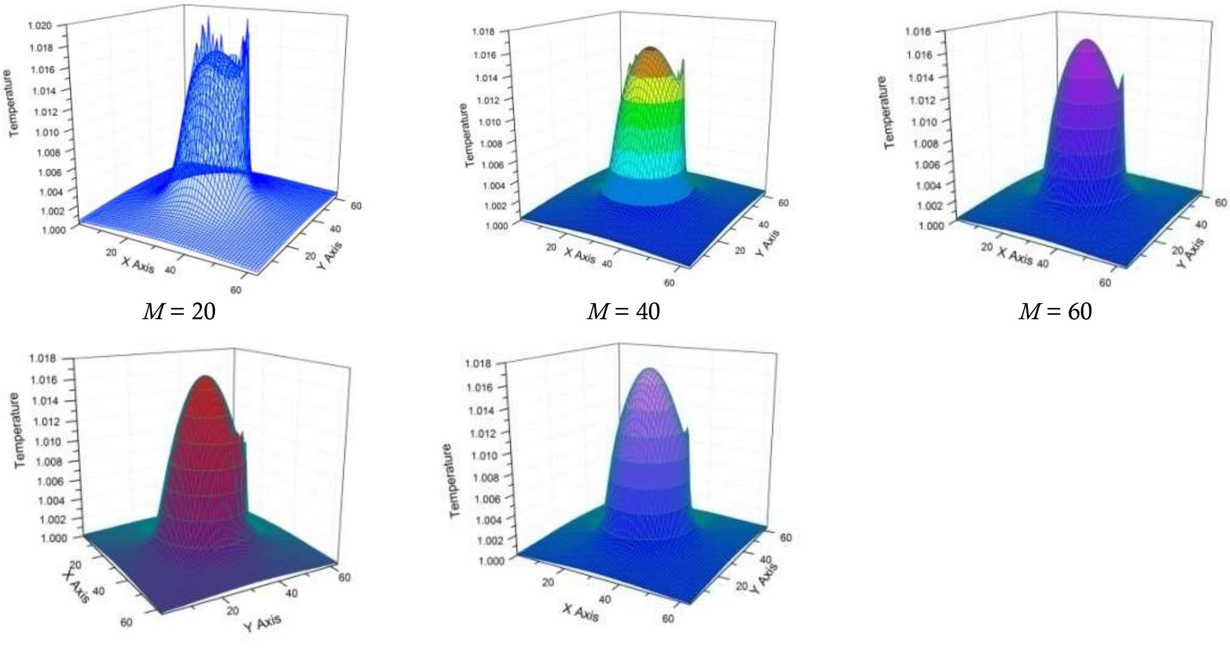

$M = 20$ $M = 40$ $M = 60$

$M = 80$ $M = 100$

Figure 8. Mid-film temperature distributions for varying load from $M = 20$ to 100 with the constant speed $L = 12.04$.

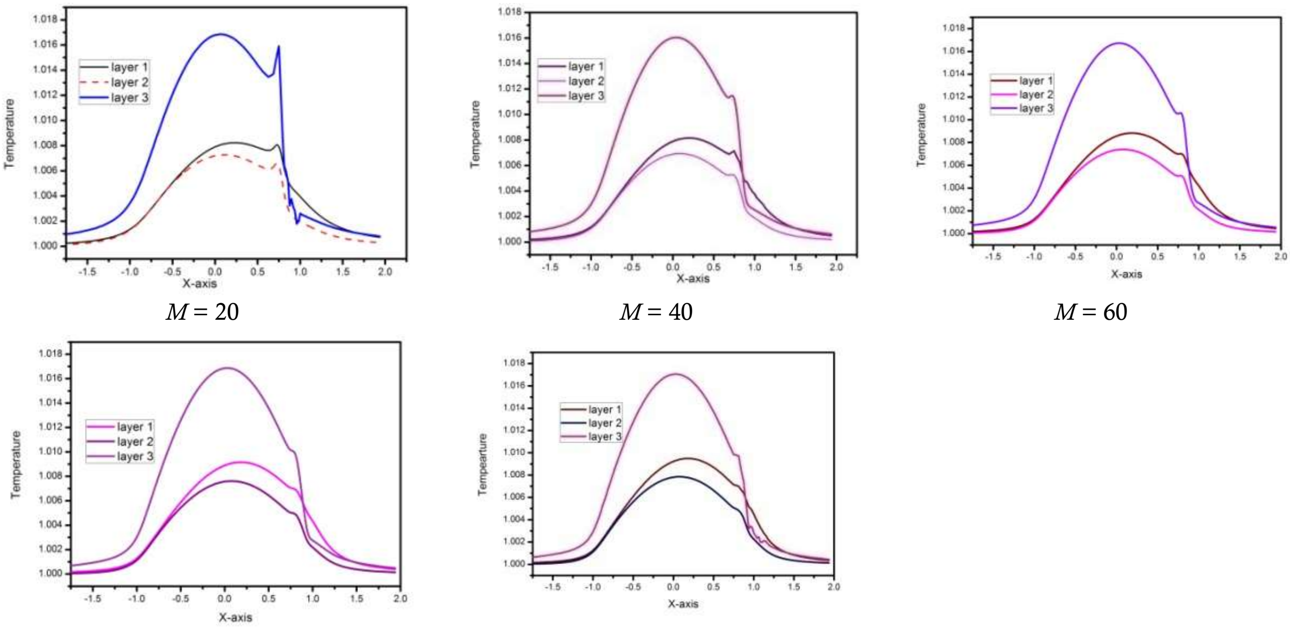

$M = 20$ $M = 40$ $M = 60$

$M = 80$ $M = 100$

Figure 9. Layer-wise temperature profiles for varying load from $M = 20$ to 100 with the constant speed $L = 12.04$.

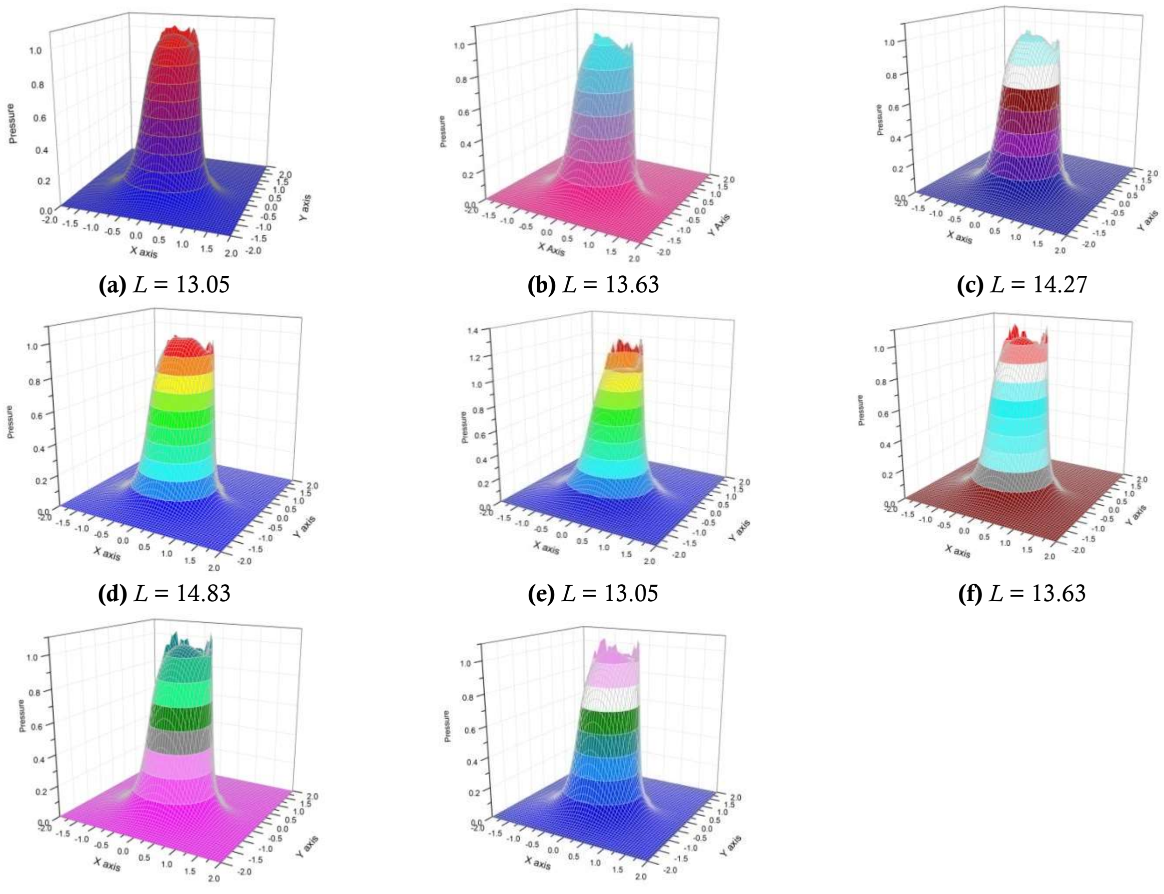

(a) L = 13.05 **(b)** L = 13.63 **(c)** L = 14.27

(d) L = 14.83 **(e)** L = 13.05 **(f)** L = 13.63

(g) L = 14.27 **(h)** L = 14.83

Figure 10. (a)–(d) represents the isothermal pressure profiles; and **(e)–(h)** represents thermal pressure profiles for varying speed from L = 13.05, 13.63, 14.27 and 14.83 with constant load M = 20.

The isothermal as well as thermal film thickness distributions are depicted in **Figure 11**, for varying speed with constant load and slide-to-roll ratio $L = 13.05, 13.63, 14.27, 14.83. M = 20$, SR $= 0.25$ respectively, also shows the occurrence of dimple. The minimum and central film thickness decrease as the speed increases. The contour plots of isothermal and thermal film thickness are exemplified in **Figure 12**. It displays the horse shoe constriction that is noticed; also, isothermal, thermal pressure, and film thickness profiles for varying speeds are represented in **Figure 13**. It is observed that the pressure spike increases with an increase in speed. Mid-film temperature profiles are described in **Figure 14,** and layer-wise surface mid-film temperatures are also demonstrated.

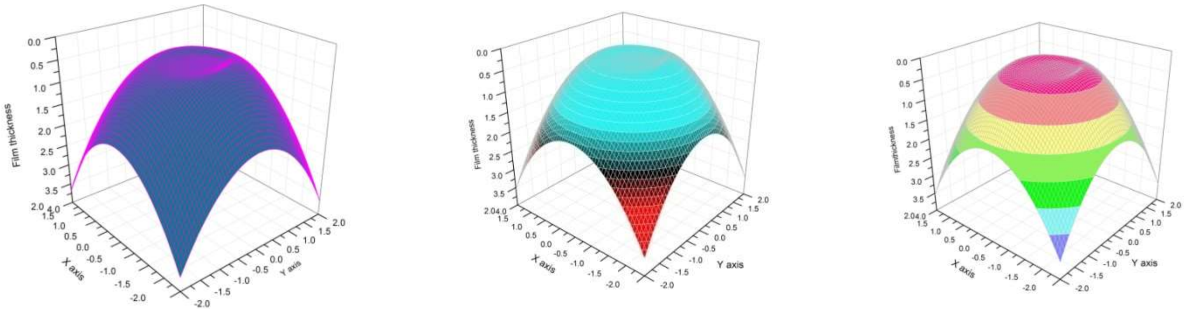

(a) L = 13.05 **(b)** L = 13.63 **(c)** L = 14.27

Figure 11. (*Continued*).

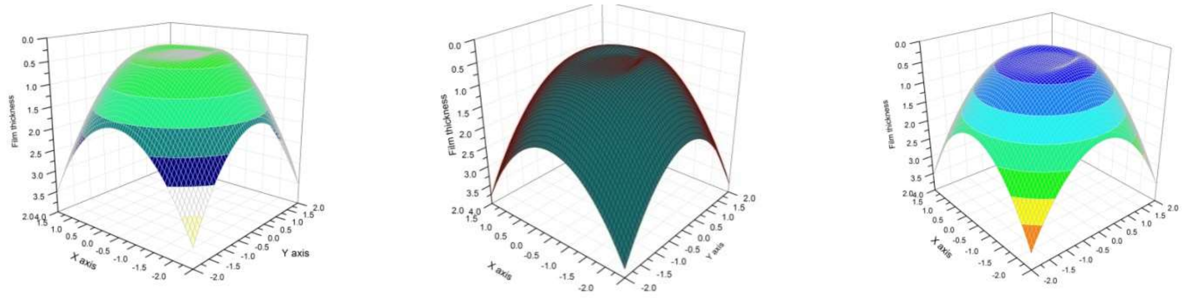

(d) L = 14.83 **(e)** L = 13.05 **(f)** L = 13.63

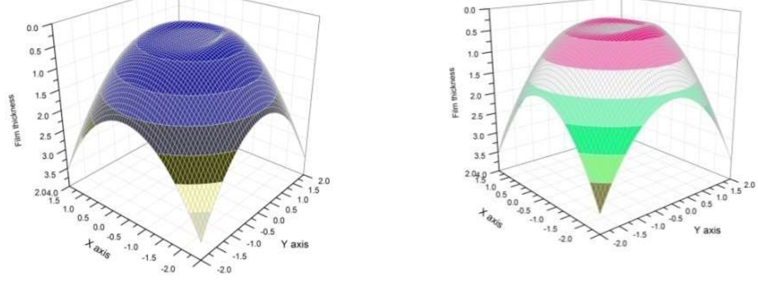

(g) L = 14.27 **(h)** L = 14.83

Figure 11. (a)–(d) represents the isothermal film thickness profiles; and **(e)–(h)** represents thermal film thickness profiles for varying speed from L = 13.05, 13.63, 14.27 and 14.83, with constant load M = 20.

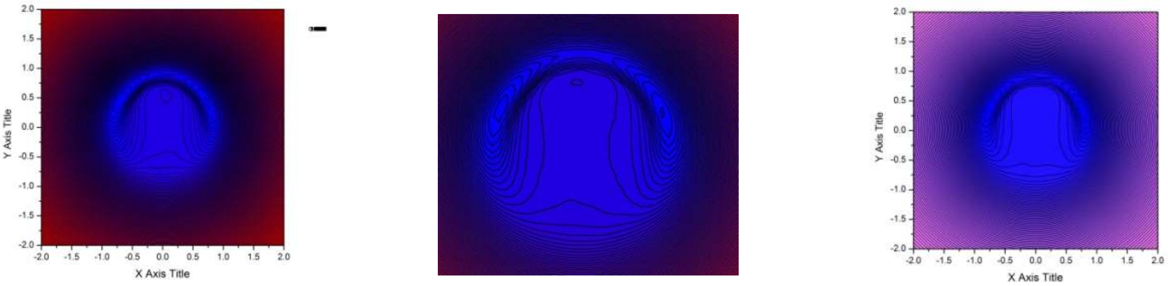

(a) L = 13.05 **(b)** L = 13.63 **(c)** L = 14.27

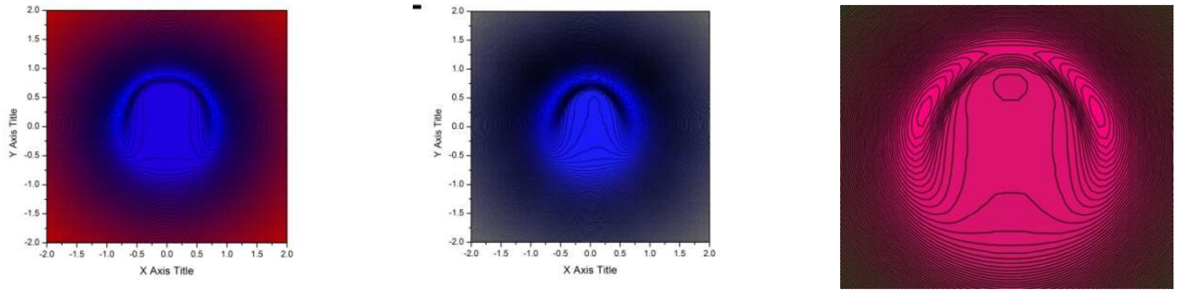

(d) L = 14.83 **(e)** L = 13.05 **(f)** L = 13.63

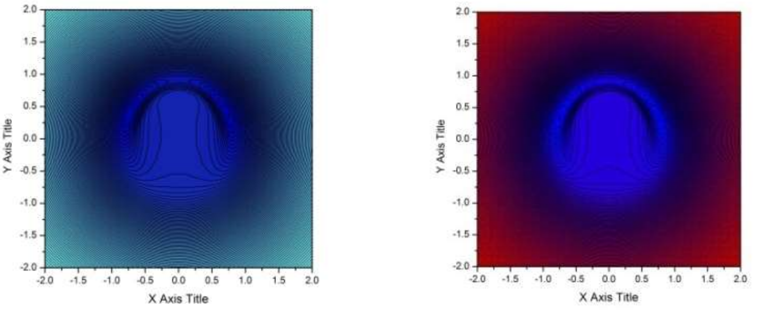

(g) L = 14.27 **(h)** L = 14.83

Figure 12. (a)–(d) represents the contour plots of isothermal film thickness profiles; and **(e)–(h)** represents contour plots of thermal film thickness profiles for varying speed from L = 13.05, 13.63, 14.27 and 14.83, with constant load M = 20.

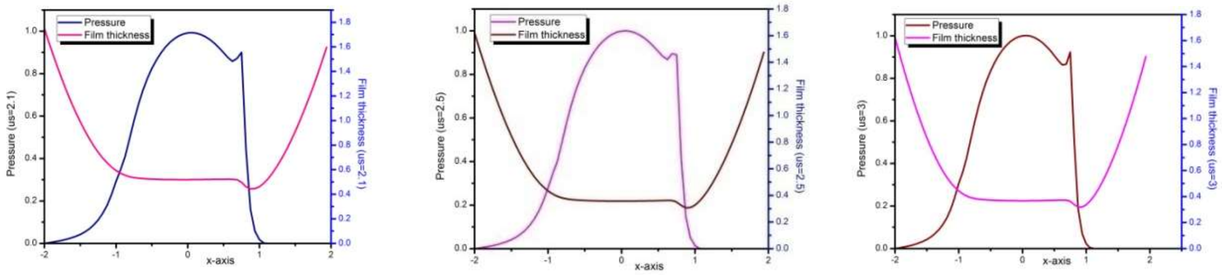

(a) L = 13.05 **(b)** L = 13.63 **(c)** L = 14.27

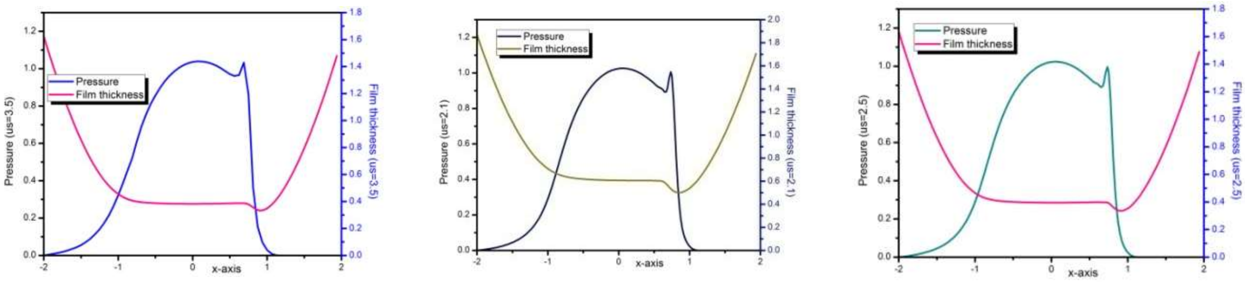

(d) L = 14.83 **(e)** L = 13.05 **(f)** L = 13.63

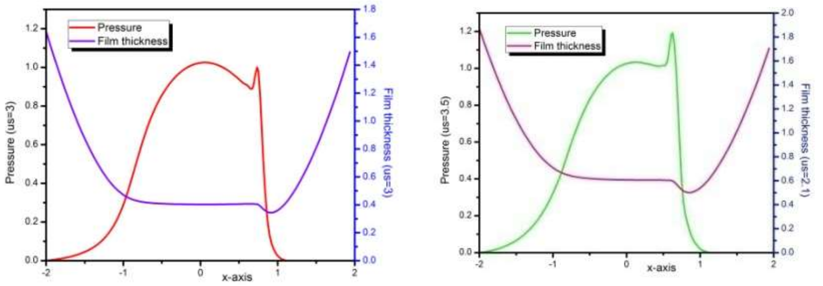

(g) L = 14.27 **(h)** L = 14.83

Figure 13. (a)–(d) represents the isothermal pressure and film thickness profiles; and **(e)–(h)** represents thermal pressure and film thickness profiles for varying speed from L = 13.05, 13.63, 14.27 and 14.83, with constant load M = 20.

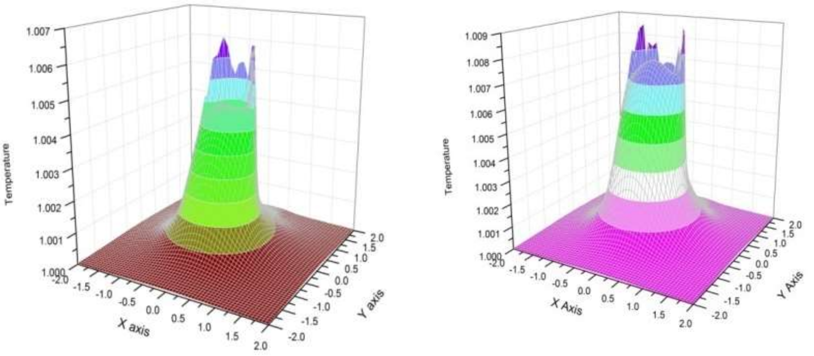

L = 13.05 L = 13.63

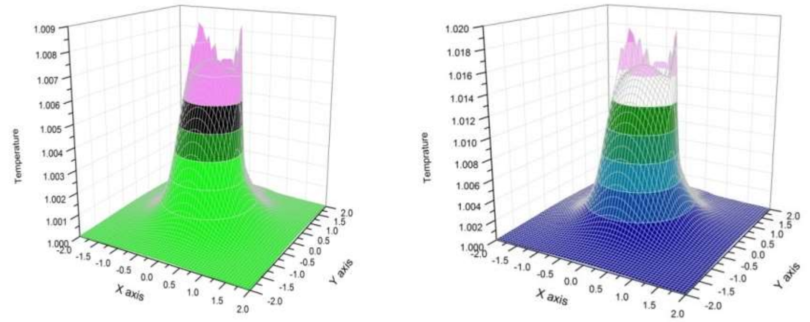

L = 14.27 L = 14.83

Figure 14. Mid-film temperature profiles for varying speed from L = 13.05, 13.63, 14.27 and 14.83, with constant load M = 20.

The surface roughness is included in the present computation, i.e., $\bar{A}\, cos\left(\frac{2\pi X'}{\hat{W}}\right)$, where $\bar{A} = 0.495 \times 10^{-06}$ the amplitude is $\hat{W} = 0.25 \times 10^{-03}$ is the dimensionless wavelength. The waviness is oriented at 45° to the direction of entrainment under thermal conditions with SR = 0.25. Ehret et al.[54] considered only isothermal cases and studied the effect of waviness on film thickness under high load with pure sliding conditions. It is examined that the effect of waviness under thermal conditions and SR. The isothermal and thermal pressure profiles for various load $M = 126, 150, 200, 350, 500$ with SR = 0.25 are inspected and described in **Figures 15** and **16**. It shows that the ridges and pressure spike appear at the outlet region. The contour plots of isothermal and thermal film thickness distributions are illustrated in **Figures 17** and **18** respectively. Actually, waviness describes flow at the entrance of the contact and lubricant leakage flow which accumulates at the entrance. The layer-wise temperature profiles are depicted in **Figure 19**, and it depicts that finger-like projections in the temperature profiles.

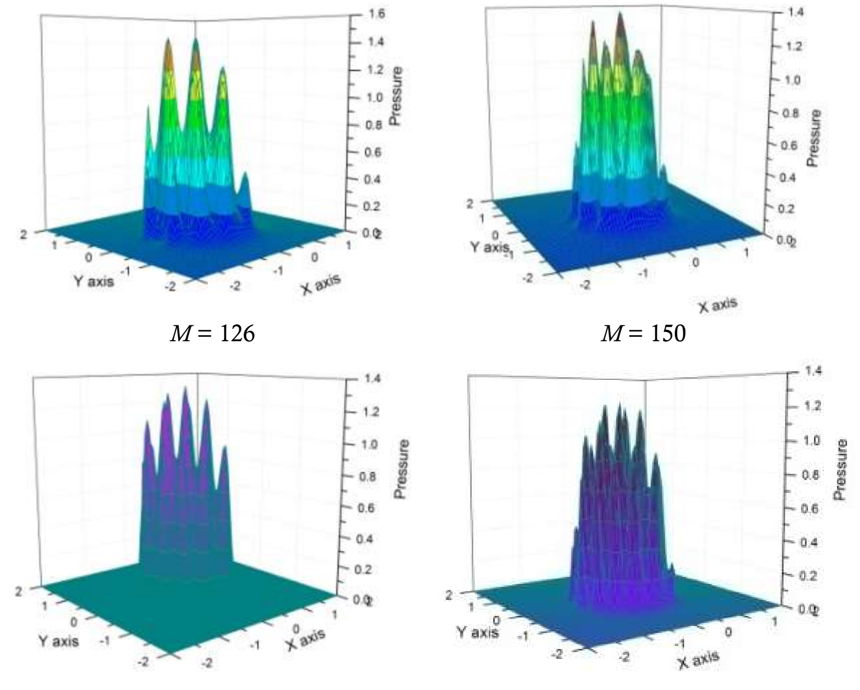

M = 126 *M* = 150 *M* = 200

M = 350 *M* = 500

Figure 15. Isothermal pressure distributions for various load *M* = 126, 150, 200, 350, 500 with the constant speed *L* = 12.34 and surface roughness.

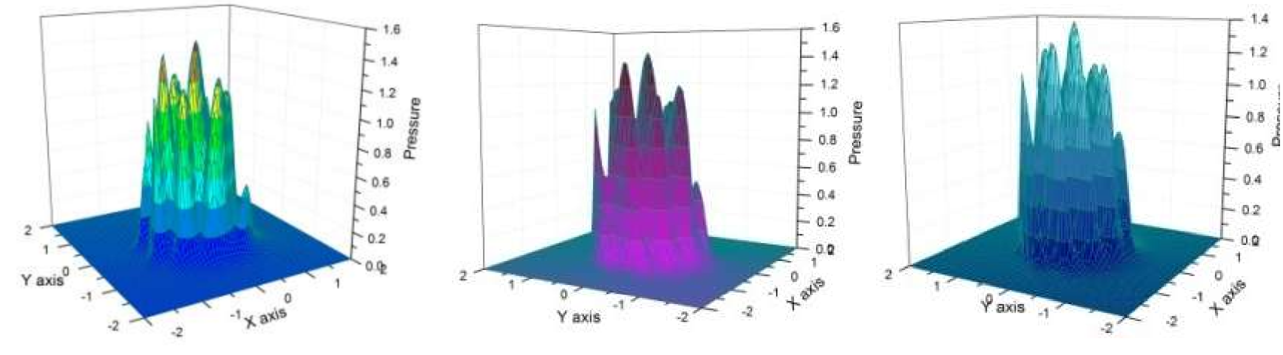

M = 126 *M* = 150 *M* = 200

Figure 16. (*Continued*).

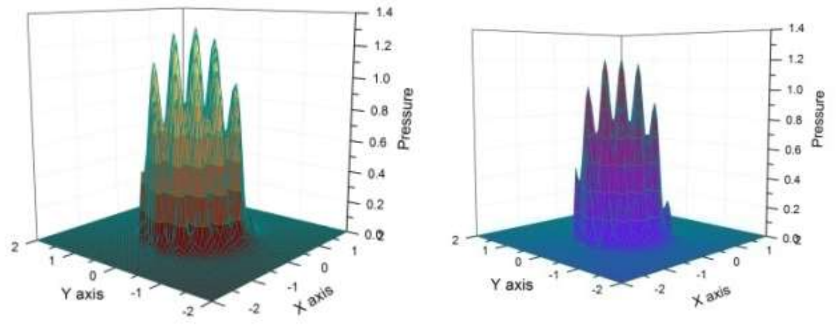

M = 350 *M* = 500

Figure 16. Thermal pressure distributions for various load *M* = 126, 150, 200, 350, 500 with the constant speed *L* = 12.34 and surface roughness.

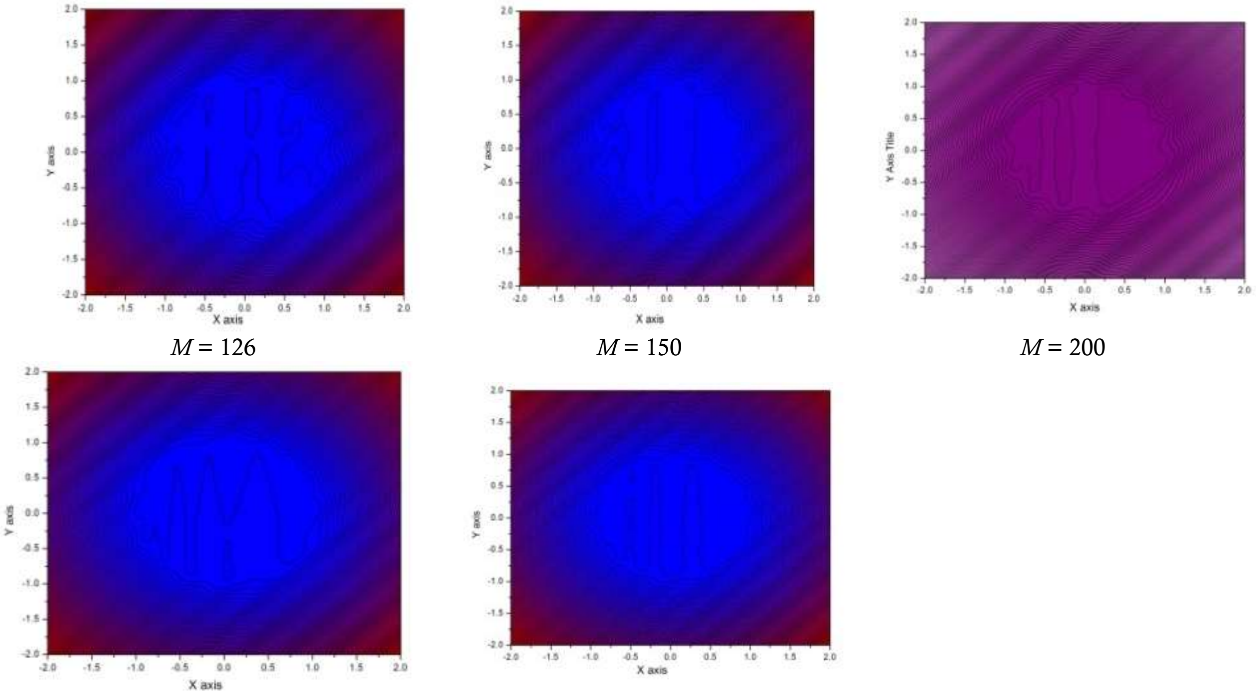

M = 126 *M* = 150 *M* = 200

M = 350 *M* = 500

Figure 17. Contour plot of isothermal film thickness for various load *M* = 126, 150, 200, 350, 500 with the constant speed *L* = 12.34 and surface roughness.

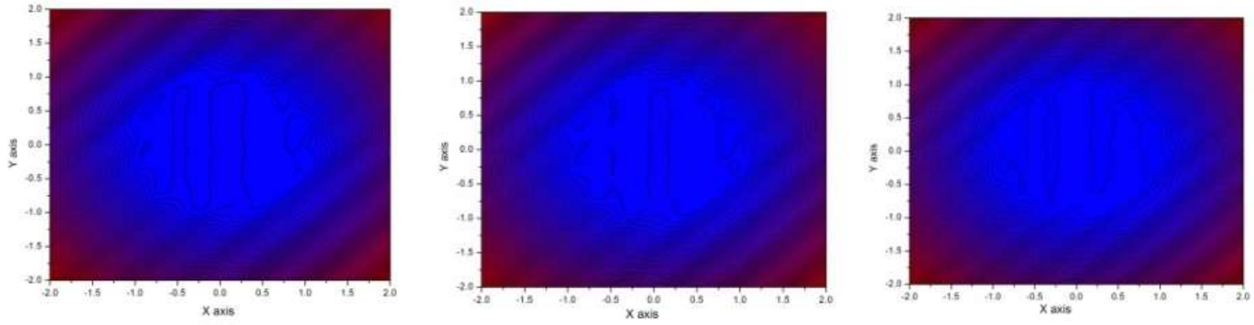

M = 126 *M* = 150 *M* = 200

Figure 18. (*Continued*).

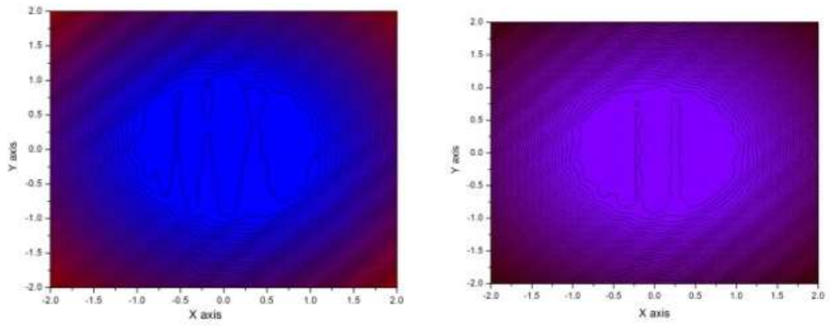

M = 350 *M* = 500

Figure 18. Contour plot of thermal film thickness for various load *M* = 126, 150, 200, 350, 500 with the constant speed *L* = 12.34 and surface roughness.

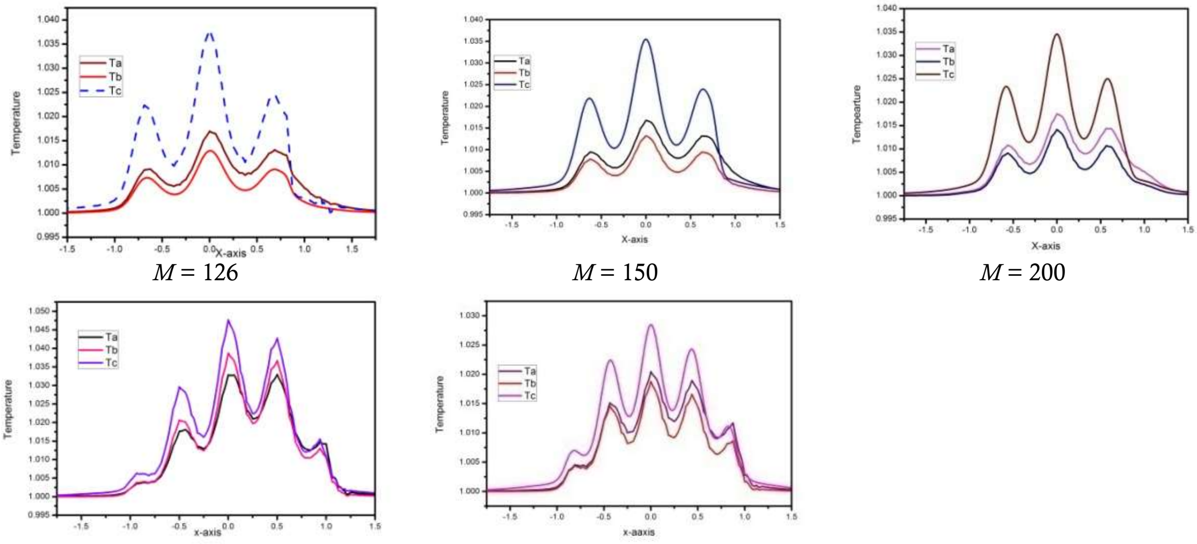

M = 126 *M* = 150 *M* = 200

M = 350 *M* = 500

Figure 19. Layer-wise temperature profiles for various load *M* = 126, 150, 200, 350, 500 with the constant speed *L* = 12.34 and surface roughness.

The effect of slide-to-roll ratio on fluid film thickness is discussed for SR = −1, −0.5, 0, 0.5, 1. The contour plots of isothermal and thermal film thickness profiles are illustrated in **Figures 20** and **21,** respectively. It predicts that the minimum film thickness is much smaller when the slide-to-roll ratio is positive as compared to negative. Whereas central film thickness contrasts to that of minimum film thickness, is described in **Table 3**. It is perceived that the position of minimum film thickness in the contour plots, when slide-to-roll ratio is negative, is located at the side lobes of horse shoe shaped constriction. As the slide-to-roll ratio becomes positive, the location of the minimum film thickness shifts towards the back of the horse shoe constriction. The isothermal and thermal pressure profiles are exemplified respectively in **Figures 22** and **23**, and mid-film temperature distributions are depicted in **Figure 24**. The load $M = 57.21$ with speed $L = 10.52$, when the slide to roll ratio increases from 0.5 to 1, the pressure spike and central pressure increase due to the action of the temperature-viscosity wedge term, and there is the occurrence of another peak. Also, central pressure and pressure spike values are smaller when slide-to-roll ratio is negative. The occurrence and action of temperature-viscosity wedge action is purely governed by EHL pressure spike.

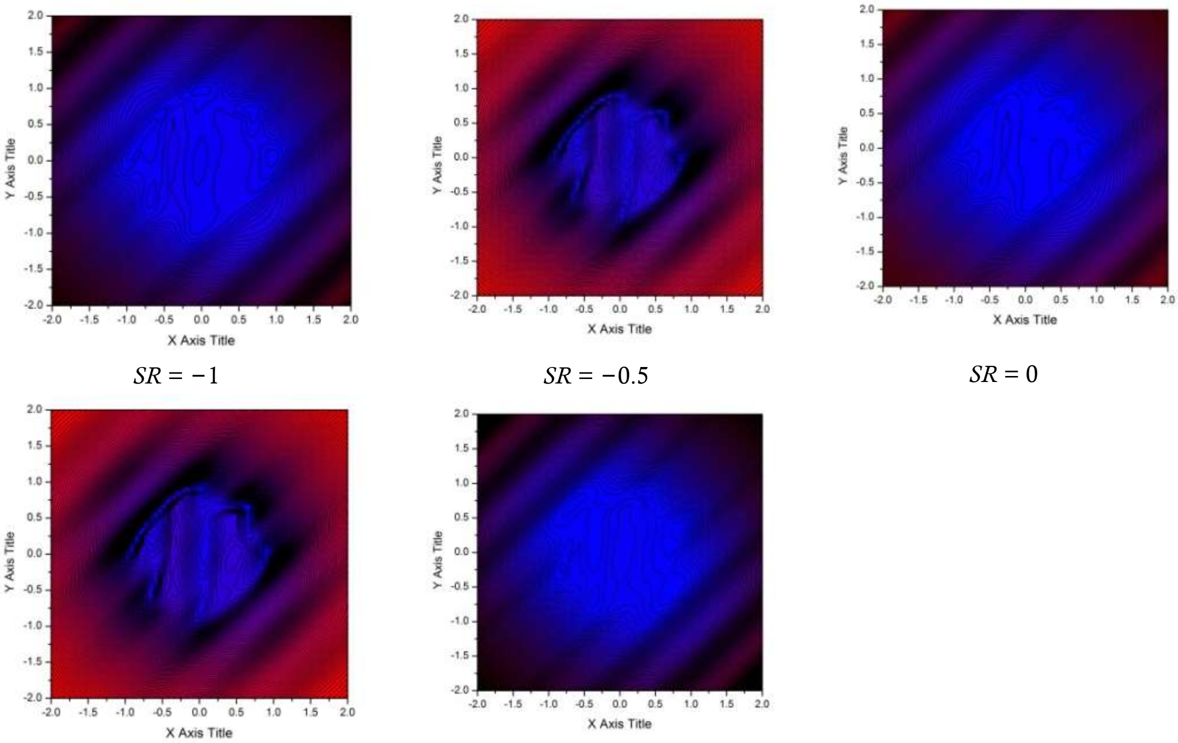

$SR = -1$ $SR = -0.5$ $SR = 0$

$SR = 0.5$ $SR = 1$

Figure 20. Contour plot of isothermal film thickness for various slide to roll ratio at constant load and speed with surface roughness.

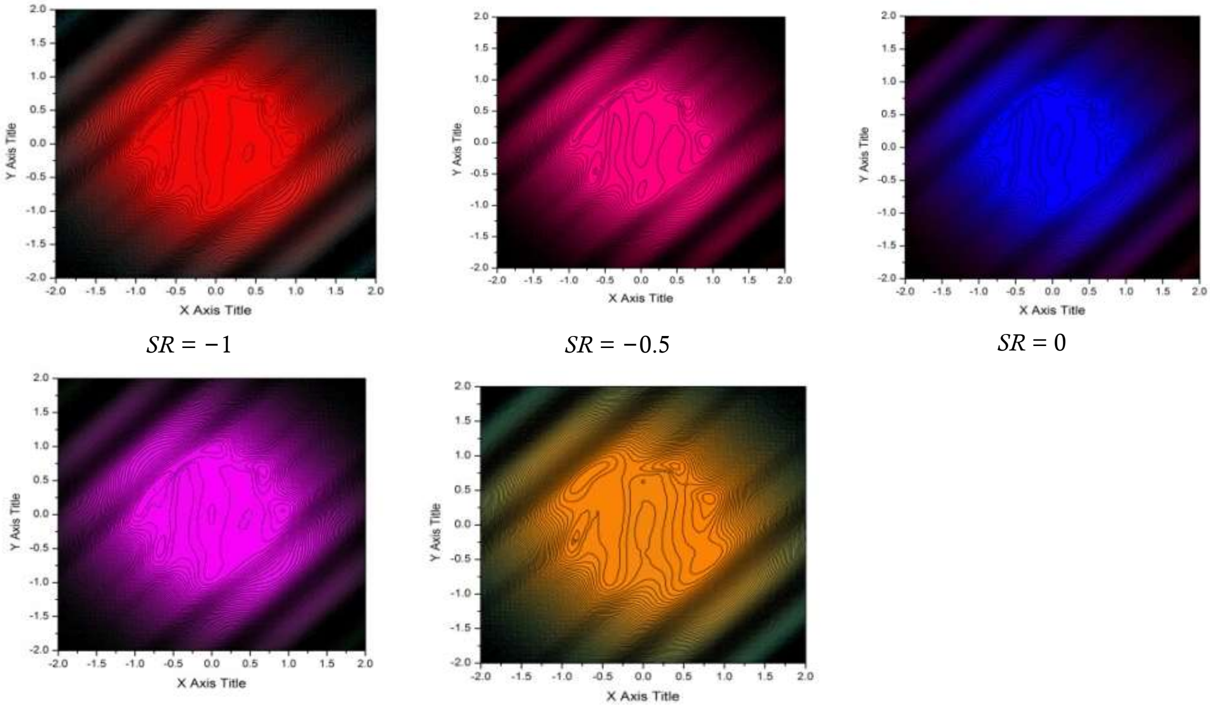

$SR = -1$ $SR = -0.5$ $SR = 0$

$SR = 0.5$ $SR = 1$

Figure 21. Contour plot of thermal film thickness for various slide to roll ratio at constant load and speed with surface roughness.

Table 3. Comparison of isothermal and thermal film thickness for various slide to roll ratios.

Slide to roll ratio (SR)	**Isothermal film thickness**		**Thermal film thickness**	
	$\mathbf{H_{min}}$	$\mathbf{H_{cen}}$	$\mathbf{H_{min}}$	$\mathbf{H_{cen}}$
−1	0.1683	0.2433	0.0818	0.1783
−0.5	0.1669	0.2405	0.1498	0.2428
0	0.1687	0.2437	0.1684	0.2597
0.5	0.1650	0.2372	0.1530	0.2449
1	0.1669	0.2405	0.1117	0.2058

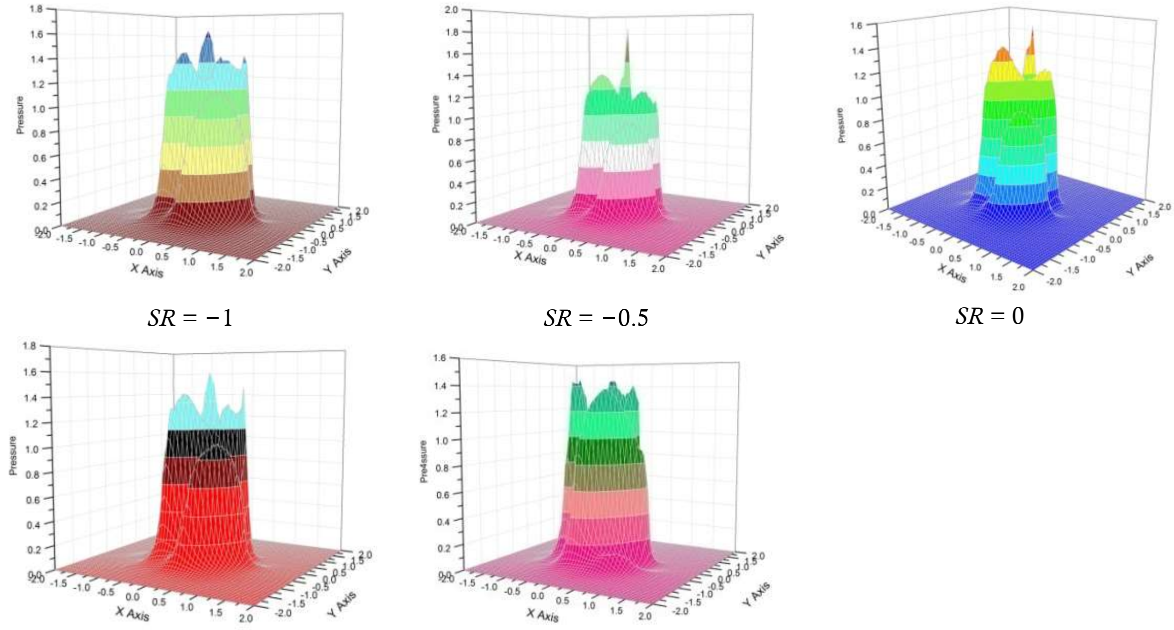

SR = −1 *SR* = −0.5 *SR* = 0

SR = 0.5 *SR* = 1

Figure 22. Isothermal pressure distributions for various slide to roll ratio at constant load and speed with surface roughness.

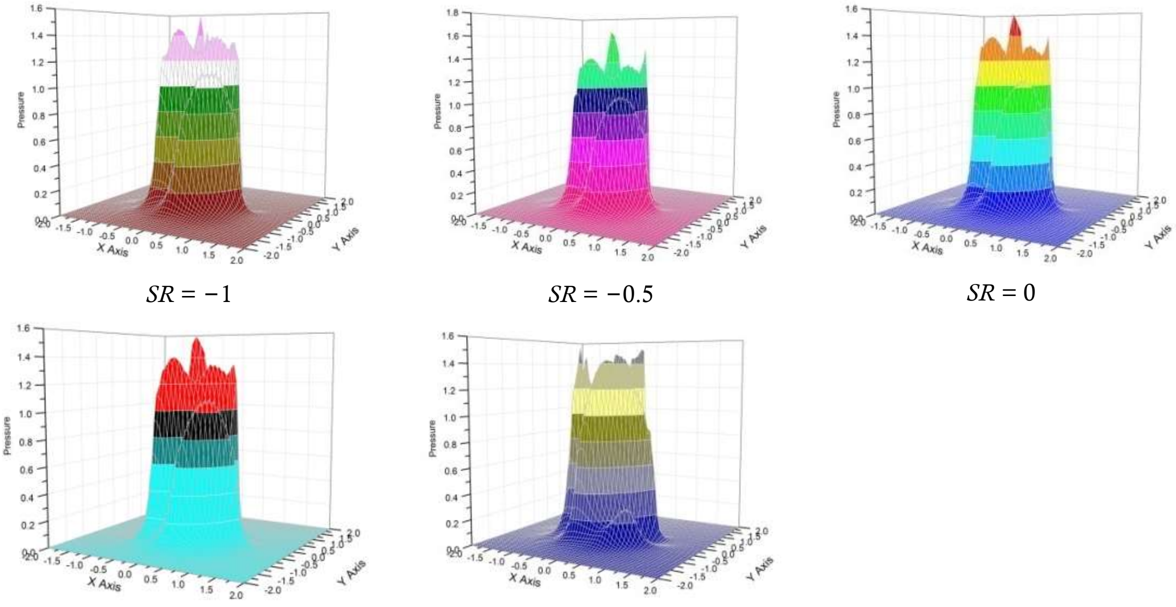

SR = −1 *SR* = −0.5 *SR* = 0

SR = 0.5 *SR* = 1

Figure 23. Thermal pressure profiles for various slide to roll ratio at constant load and speed with surface roughness.

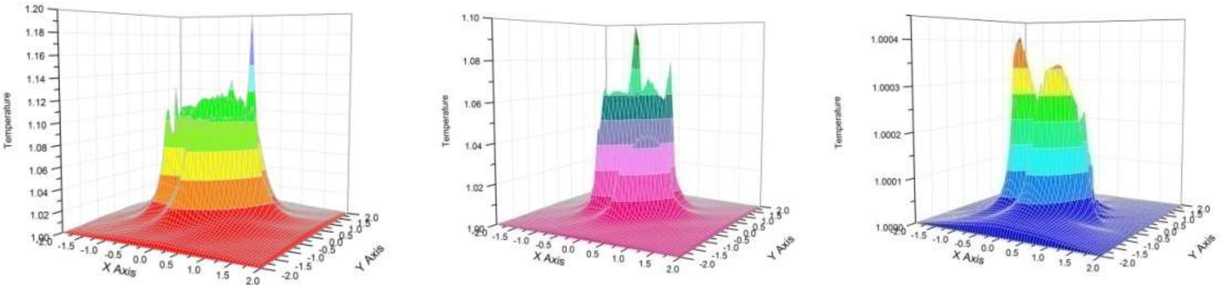

SR = −1 *SR* = −0.5 *SR* = 0

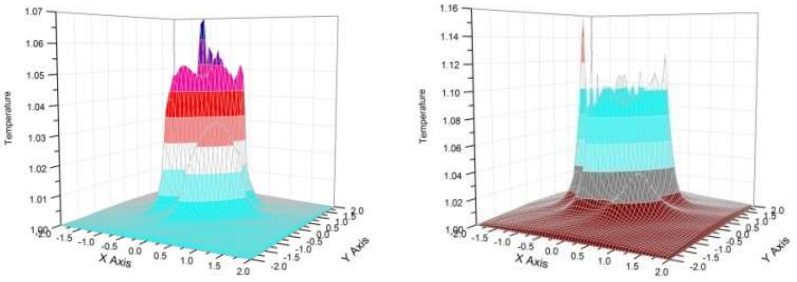

SR = 0.5 *SR* = 1

Figure 24. Mid-film temperature distributions for various slide to roll ratio at constant load and speed with surface roughness.

5. Conclusions

From the above study, the following conclusions are drawn:

1) The pressure spike and film thickness decrease with an increase in load, whereas pressure spike and film thickness increase with an increase in speed.
2) Isothermal minimum film thickness is larger than the thermal minimum film thickness due to a rise in the temperature at the contact region.
3) Surface temperature distribution is smaller as compared to contact temperature distribution.
4) When the slide-to-roll ratio is positive, the pressure spike and central pressure profiles increase due to the action of the temperature-viscosity wedge term, and there is the occurrence of another peak. Also, the central pressure and pressure spike values are smaller when the slide-to-roll ratio is negative.
5) Minimum film thickness is much smaller when slide-to-roll ratio is positive as compared to negative, whereas central film thickness behavior is contrasted to that of minimum film thickness.

Author contributions

Conceptualization, VBA; methodology, VBA, PMO and MKN; validation, VBA, PMO and MKN; formal analysis, PMO and MKN; investigation, VBA, PMO and MKN; writing—original draft preparation, VBA, PMO and MKN; writing—review and editing, VBA, PMO and MKN; supervision, VBA. All authors have read and agreed to the published version of the manuscript.

Conflict of interest

The authors declare no conflict of interest.

References

1. Crook AW. The lubrication of rollers III. A theoretical discussion of friction and the temperatures in the oil film. *Philosophical Transactions of the Royal Society A: Mathematical, Physical and Engineering Sciences* 1961; 254(1040): 237–258.doi: 10.1098/rsta.1961.0016

2. Sternlicht B, Lewis P, Flynn P. Theory of lubrication and failure of rolling contacts. *Journal of Basic Engineering* 1961; 83(2): 213–222. doi: 10.1115/1.3658927
3. Cheng HS, Sternlicht B. A numerical solution for the pressure, temperature, and film thickness between two infinitely long, lubricated rolling and sliding cylinders, under heavy loads. *Journal of Basic Engineering* 1965; 87(3): 695–704.doi: 10.1115/1.3650647
4. Dowson D, Whitaker AV. Paper 4: A numerical procedure for the solution of the elastohydrodynamic problem of rolling and sliding contacts lubricated by a Newtonian fluid. *Proceedings of the Institution of Mechanical Engineers* 1965; 180(2): 57–71.doi: 10.1243/PIME_CONF_1965_180_064_0
5. Murch LE, Wilson WRD. A thermal elastohydrodynamic inlet zone analysis. *Journal of Lubrication Technology* 1975; 97(2): 212–216. doi: 10.1115/1.3452559
6. Bruggemann H, Kollmann FG. A numerical solution of the thermal elastohydrodynamic lubrication in an elliptical contact. *Journal of Lubrication Technology* 1982; 104(3): 392–400. doi: 10.1115/1.3253231
7. Kim KH, Sadeghi F. Three-dimensional temperature distribution in EHD lubrication: Part I—Circular contact. *Journal of Tribology* 1992; 114(1): 32–41. doi: 10.1115/1.2920864
8. Kim KH, Sadeghi F. Three-dimensional temperature distribution in EHD lubrication: Part II—Point contact and numerical formulation. *Journal of Tribology* 1993; 115(1): 36–45. doi: 10.1115/1.2920984
9. Salehizadeh H, Saka N. Thermal non-Newtonian elastohydrodynamic lubrication of rolling line contacts. *Journal of Tribology* 1991; 113(3): 481–491.doi: 10.1115/1.2920649
10. Wolff R, Kubo A. The application of Newton-Raphson method to thermal elastohydrodynamic lubrication of line contacts. *Journal of Tribology* 1994; 116(4): 733–740.doi: 10.1115/1.2927327
11. Kazama T, Ehret P, Taylor CM. On the effects of the temperature profile approximation in thermal Newtonian solutions of elastohydrodynamic lubrication line contacts. *Proceedings of the Institution of Mechanical Engineers, Part J: Journal of Engineering Tribology* 2001; 215(1): 109–120.doi: 10.1243/1350650011541666
12. Lee RT, Hsu CH, Kuo WF. Multilevel solution for thermal elastohydrodynamic lubrication of rolling/sliding circular contacts. *Tribology International* 1995; 28(8): 541–552. doi: 10.1016/0301-679X(96)85542-3
13. Ehret P, Dowson D, Taylor CM. Thermal effects in elliptical contacts with spin conditions. *Tribology Series* 1999; 36: 685–703. doi: 10.1016/S0167-8922(99)80088-1
14. Qu S, Yang P, Guo F. Theoretical investigation on the dimple occurrence in the thermal EHL of simple sliding steel-glass circular contacts. *Tribology International* 2000; 33(1): 59–65.doi: 10.1016/S0301-679X(00)00031-1
15. Yang P, Qu S, Kaneta M, Nishikawa H. Formation of steady dimples in point TEHL contacts. *Journal of Tribology* 2001; 123(1): 42–49.doi: 10.1115/1.1332399
16. Guo F, Yang P, Qu S. On the theory of thermal elastohydrodynamic lubrication at high slide-roll ratios—Circular glass-steel contact solution at opposite sliding. *Journal of Tribology* 2001; 123(4): 816–821. doi: 10.1115/1.1330739
17. Kim HJ, Ehret P, Dowson D, Taylor CM. Thermal elastohydrodynamic analysis of circular contacts part 1: Newtonian model. *Proceedings of the Institution of Mechanical Engineers, Part J: Journal of Engineering Tribology* 2001; 215(4): 339–352.doi: 10.1243/1350650011543583
18. Kim HJ, Ehret P, Dowson D, Taylor CM. Thermal elastohydrodynamic analysis of circular contacts part 2: Non-Newtonian model. *Proceedings of the Institution of Mechanical Engineers, Part J: Journal of Engineering Tribology* 2001; 215(4): 353–362. doi: 10.1243/1350650011543592
19. Cann PM, Spikes HA. Determination of the shear stress of lubricants in elastohydrodynamic contacts. *Tribology Transactions* 1989; 32(3): 414–422. doi: 10.1080/10402008908981908
20. Liu X, Jiang M, Yang P, Kaneta M. Non-Newtonian thermal analyses of point EHL contacts using the Eyring model. *Journal of Tribology* 2005; 127(1): 70–81. doi: 10.1115/1.1843161
21. Greenwood JA, Williamson JBP. Contact of nominally flat surfaces. *Proceedings of the Royal Society A: Mathematical, Physical and Engineering Sciences* 1966; 295(1442): 300–319. doi: 10.1098/rspa.1966.0242
22. Greenwood JA, Tripp JH. The contact of two nominally flat rough surfaces. *Proceedings of the Institution of Mechanical Engineers* 1970; 185(1): 625–633.doi: 10.1243/PIME_PROC_1970_185_069_02
23. Patir N, Cheng HS. An average flow model for determining effects of three-dimensional roughness on partial hydrodynamic lubrication. *Journal of Lubrication Technology* 1978; 100(1): 12–17. doi: 10.1115/1.3453103
24. Sadeghi, F, Sui PC. Thermal elastohydrodynamic lubrication of rough surfaces. *Journal of Tribology* 1990; 112(2): 341–346. doi: 10.1115/1.2920262
25. Chang L. A deterministic model for line-contact partial elastohydrodynamic lubrication. *Tribology International* 1995; 28(2): 75–84.doi: 10.1016/0301-679X(95)92697-4
26. Hu YZ, Zhu D. A full numerical solution to the mixed lubrication in point contacts. *Journal of Tribology* 2000; 122(1): 1–9. doi: 10.1115/1.555322

27. Wang QJ, Zhu D, Cheng HS, et al. Mixed lubrication analyses by a macro-micro approach and a full-scale mixed EHL model. *Journal of Tribology* 2004; 126(1): 81–91. doi: 10.1115/1.1631017
28. Lu X, Khonsari MM, Gelinck ERM. The stribeck curve: Experimental results and theoretical prediction. *Journal of Tribology* 2006; 128(4): 789–794. doi: 10.1115/1.2345406
29. Deolalikar N, Sadeghi F, Marble S. Numerical modeling of mixed lubrication and flash temperature in EHL elliptical contacts. *Journal of Tribology* 2008; 130(1): 011004. doi: 10.1115/1.2805429
30. Yang P, Cui J, Jin ZM, Dowson D. Influence of two-sided surface waviness on the EHL behavior of rolling/sliding point contacts under thermal and non-Newtonian conditions. *Journal of Tribology* 2008; 130(4): 041502. doi: 10.1115/1.2958078
31. Akbarzadeh S, Khonsari MM. Performance of spur gears considering surface roughness and shear thinning lubricant. *Journal of Tribology* 2008; 130(2): 021503. doi: 10.1115/1.2805431
32. Sojoudi H, Khonsari MM. On the behavior of friction in lubricated point contact with provision for surface roughness. *Journal of Tribology* 2010; 132(1): 012102. doi: 10.1115/1.4000306
33. Zhu D, Wang QJ. Effect of roughness orientation on the elastohydrodynamic lubrication film thickness. *Journal of Tribology* 2013; 135(3): 031501.doi: 10.1115/1.4023250
34. Masjedi M, Khonsari MM. On the effect of surface roughness in point-contact EHL: Formulas for film thickness and asperity load. *Tribology International* 2015; 82(A): 228–244. doi: 10.1016/j.triboint.2014.09.010
35. Awati VB, Naik S, Kumar M. Multigrid method for the solution of EHL point contact with bio-based oil as lubricants for smooth and rough asperity. *Industrial Lubrication and Tribology* 2018; 70(4): 599–611.doi: 10.1108/ILT-12-2016-0314
36. Zhang B, Wang J, Omasta M, Kaneta M. Variation of surface dimple in point contact thermal EHL under ZEV condition. *Tribology International* 2016; 94: 383–394.doi: 10.1016/j.triboint.2015.09.036
37. Cui J, Yang P, Kaneta M, Krupka I. Numerical study on the interaction of transversely oriented ridges in thermal elastohydrodynamic lubrication point contacts using the Eyring shear-thinning model. *Proceedings of the Institution of Mechanical Engineers, Part J: Journal of Engineering Tribology* 2017; 231(1): 93–106.doi: 10.1177/1350650116646943
38. Awati VB, Kumar NM, Bujurke NM. Numerical solution of thermal EHL line contact with bio-based oil as lubricant. *Australian Journal of Mechanical Engineering* 2022; 20(1): 231–244.doi: 10.1080/14484846.2019.1699720
39. Liu X, Cui J, Yang P. Size effect on the behavior of thermal elastohydrodynamic lubrication of roller pairs. *Journal of Tribology* 2012; 134(1): 011502. doi: 10.1115/1.4005515
40. Hultqvist T, Vrcek A, Marklund P, et al. Transient analysis of surface roughness features in thermal elastohydrodynamic contacts. *Tribology International* 2019; 141: 10595.doi: 10.1016/j.triboint.2019.105915
41. Zhao Y, Wong PL, Mao JH. Solving coupled boundary slip and heat transfer EHL problem under large slide-roll ratio conditions. *Tribology International* 2019; 133: 73–87.doi: 10.1016/j.triboint.2019.01.013
42. Zhang M, Wang J, Yang P, et al. A thermal EHL investigation for size effect of finite line contact on bush-pin hinge pairs in industrial chains. *Industrial Lubrication and Tribology* 2019; 72(5): 695–701.doi: 10.1108/ILT-10-2019-0448
43. Zhang M, Wang J, Cui J, Yang P. A thermal investigation on plate-pin hinge pairs in silent chains using a narrow finite line contact. *Industrial Lubrication and Tribology* 2020; 72(10): 1139–1145. doi: 10.1108/ILT-11-2019-0498
44. Zhao Y, Wong PL. Thermal-EHL analysis of slip/no-slip contact at high slide-to-roll ratio. *Tribology International* 2021; 153: 106617. doi: 10.1016/j.triboint.2020.106617
45. Brandt A. Multi-level adaptive solutions to boundary-value problems. *Mathematics of Computation* 1977; 31(138): 333–390.
46. Lubrecht AA, ten Napel WE, Bosma R. Multigrid, an alternative method of solution for two-dimensional elastohydrodynamically lubricated point contact calculations. *Journal of Tribology* 1987; 109(3): 437–443.doi: 10.1115/1.3261467
47. Venner C. *Multilevel Solution of the EHL Line and Point Contact Problems* [PhD thesis]. University of Twente; 1991.
48. Roelands CJA, Winer WO, Wright WA. Correlational aspects of the viscosity-temperature-pressure relationship of lubricating oils. (Dr In dissertation at Technical University of Delft, 1966). *Journal of Lubrication Technology* 1971; 93(1): 209–210.doi: 10.1115/1.3451519
49. Dowson D, Higginson GR. *Elasto-Hydrodynamic Lubrication: The Fundamentals of Roller Gear Lubrication*. Pergamon Press; 1966.
50. Pai SI. *Viscous Flow Theory, Vol. 1 (One): Laminar Flow. D*. Van Nostrand Company; 1956.
51. Liu J. *Thermal Non-Newtonian Elastohydrodynamic Lubrication of Point Contacts* [PhD thesis]. The University of Leeds; 1994.
52. Venner CH, Lubrecht AA. *Multi-Level Methods in Lubrication*. Elsevier; 2000.

53. Hamrock BJ, Dowson D. Isothermal elastohydrodynamic lubrication of point contacts: Part 3—Fully flooded results. *Journal of Lubrication Technology* 1977; 99(2): 264–275. doi: 10.1115/1.3453074
54. Ehret P, Dowson D, Taylor CM, Wang D. Analysis of isothermal elastohydrodynamic point contacts lubricated by Newtonian fluids using multigrid methods. *Proceedings of the Institution of Mechanical Engineers, Part C: Journal of Mechanical Engineering Science* 1997; 211(7): 493–508.doi: 10.1243/0954406971521881